

# Site-specific dehydration of olivines from San Carlos and Kilauea Iki

Elizabeth Ferriss, Terry Plank, Megan Newcombe, Dave Walker  
Lamont-Doherty Earth Observatory of Columbia University

## Abstract

The rate at which H<sup>+</sup> moves into, through, and out of olivine is of great interest for geologic applications such as quantifying the deep water cycle, assessing the fidelity of olivine-hosted melt inclusions as recorders of pre-eruptive melt compositions, and estimating the decompression rate of magma during volcanic eruptions. Here we conduct a series of experiments and observations on natural Fe-bearing olivine to better understand and quantify this H<sup>+</sup> movement, with a particular focus on the rate at which H<sup>+</sup> leaves olivine upon decompression. For the first time, we have carried out sequential dehydration experiments on single crystals of natural, Fe-bearing olivine polished and oriented along three crystallographic orientations. These efforts include four separate parts: (1) the partial hydration of polished blocks of xenolithic San Carlos olivine at 800°C and 1000°C, 1GPa, and oxygen fugacity (fO<sub>2</sub>) at the Ni-NiO buffer (NNO); (2) sequential dehydration of a homogeneous block of San Carlos olivine at 800°C, 1atm, and fO<sub>2</sub> of NNO-2.6; (3) sequential dehydration of a polished block of an olivine phenocryst from Kilauea Iki at 800 and 1000°C, 1 atm, and fO<sub>2</sub> held at NNO-2.6 until the final step, which was conducted at NNO+1.9; and (4) the measurement by secondary ion mass spectrometry of hydrogen zonation profiles in an olivine phenocryst from Kilauea Iki coupled with Monte Carlo modeling and known decompression rates to determine bulk H diffusivities in a natural setting. Hydrogen zonation profiles were measured in all three crystallographic directions *a*, *b*, and *c* through the uncut blocks before and after each time step for all experiments by Fourier transform infrared spectroscopy using light polarized || *a* and modeled in 3 dimensions to determine both bulk and peak-specific dehydration, producing over 50 sets of 3 apparent diffusivities.

The results show that the apparent diffusivity of bulk H<sup>+</sup> varies both over time and for olivines with different defect structures, and thus H<sup>+</sup> does not diffuse at inherently site-specific rates. These variations are due to rapid reactions that may occur between sites as a function of changing defect concentrations. Our experiments reveal three new phenomena: (1) H<sup>+</sup> that is associated with an octahedral Ti defect, [Ti-2H], can enter and exit olivine at the fastest rate measured. (2) The rate of H<sup>+</sup> loss from specific infrared absorption peaks, and in bulk, may change with progressive dehydration due to the buildup of Fe<sup>3+</sup> and redistribution of defects, particularly the rehydration of [Ti-2H]. (3) The following Arrhenius laws appear to apply to bulk H<sup>+</sup> diffusion out of most natural olivines that have been studied experimentally and naturally during dehydration: D<sub>a</sub> = 10<sup>-5.4\*</sup>exp(130/RT); D<sub>b</sub> = 10<sup>-6.9</sup>exp(130/RT); and D<sub>c</sub> = 10<sup>-6.6</sup>exp(130/RT), where R is the gas constant; the units of the diffusivities (D) are in m<sup>2</sup>/s; and the activation energy is 130 kJ/mol. This rate is slower than proton-polaron but faster than proton-metal vacancy diffusion and appears to characterize olivine of Fo~90 composition in a wide range of conditions, from self-diffusion, to melt inclusion re-equilibration, to mantle xenolith and volcanic phenocryst zonation during ascent.

## Introduction

The diffusivity of hydrogen in olivine is a fundamental physical quantity critical for understanding a wide range of earth and planetary processes. Hydrogen can affect global-scale phenomenon such as melting relations and rock strength, and so in turn may control mantle rheology and the occurrence of plate tectonics (Keppler and Smyth 2006; Bell and Rossman 1992). Accurate knowledge of the diffusivity of hydrogen also has great potential to serve as a chronometer to determine magma ascent times from

hydrogen diffusion profiles in olivine phenocrysts (Demouchy, et al., 2006). Because of its close thermodynamic relationship to water and the bonds that H<sup>+</sup> forms with oxygen within the olivine structure, hydrogen incorporated in olivine and other nominally anhydrous minerals is sometimes referred to as “water” or “hydroxyl”. Here we will primarily refer to this species as H<sup>+</sup>.

H<sup>+</sup> may be incorporated into the olivine lattice in a variety of ways that can be distinguished by differences in the absorbance of the O-H bonds as measured by Fourier transform infrared spectroscopy (FTIR) (Berry et al. 2005; Ingrin et al. 2013). Broadly, H<sup>+</sup> defects fall into two categories: relatively high wavenumber peaks associated with silicon vacancies (sometimes called Group I bands) and relatively low wavenumber peaks associated with magnesium vacancies (sometimes called Group II bands). These defects may be represented in more detail using Kröger-Vink notation, in which V is a vacancy, a superscript \* indicates a positive charge relative to an ideal crystal, ‘ indicates a negative charge relative to an ideal crystal, and <sup>x</sup> no charge difference from an ideal crystal. Subscripts indicate different sites: M for octahedral metal sites, Si for tetrahedral sites ordinarily occupied by silicon, and O for a site normally occupied by oxygen. Atoms that are not involved in any reactions are typically ignored. For example, the defect that involves a Ti<sup>4+</sup> on a metal site, 2H<sup>+</sup>, and a Si vacancy, may be represented in Kröger-Vink notation as (Ti<sup>4+</sup><sub>M</sub>)<sup>\*\*</sup>(2H<sup>+</sup><sub>T</sub>)<sup>\*</sup>. This mechanism, labeled here [Ti-2H], has been suggested to control mantle rheology (Faul et al. 2016) and manifests as a doublet of peaks at 3525 and 3573 cm<sup>-1</sup> (Berry et al. 2007). Multiple other high wavenumber peaks (3450-3620 cm<sup>-1</sup>) represent 4 H<sup>+</sup> ions charge-balanced by a Si<sup>4+</sup> vacancy, (4H<sup>+</sup>)<sub>Si</sub><sup>x</sup>, and are labeled here [Si-4H]. Some lower wavenumber peaks (3300-3400 cm<sup>-1</sup>) appear when a Mg<sup>2+</sup> vacancy is charge-balanced by a H<sup>+</sup> and a trivalent cation on a Mg<sup>2+</sup> site (Blanchard et al. 2017), (M<sup>3+</sup>)<sub>Mg</sub><sup>\*</sup>(H<sup>+</sup>)<sub>Mg</sub>', and these are labeled here [tri-H], with [tri-H-Fe<sup>3+</sup>] indicating that Fe<sup>3+</sup> is the trivalent cation and [tri-H-Al<sup>3+</sup>] indicating Al<sup>3+</sup>. Low wavenumber peaks between 3200 and 3250 cm<sup>-1</sup> have been associated with 2 H<sup>+</sup> charge-balancing a Mg<sup>2+</sup> vacancy, (2H<sup>+</sup>)<sub>Mg</sub><sup>x</sup>, and these are labeled here [Mg-2H]. The different mechanisms are important because the rate at which H<sup>+</sup> moves through the lattice may vary for each defect (Padrón-Navarta, Hermann, and O'Neill 2014).

Previous work on the diffusivity of H<sup>+</sup> in olivine has produced a 6-order-of-magnitude range of measurements, from 10<sup>-9.7</sup> m<sup>2</sup>/s during the first hour of hydrating San Carlos olivine at 1000°C (Mackwell and Kohlstedt 1990) to 10<sup>-15.7</sup> m<sup>2</sup>/s for the decrease in hydrated Si vacancies, [Si-4H], from synthetic forsterite during dehydration at the same temperature (Padrón-Navarta, Hermann, and O'Neill 2014). The calculated activation energies suggest even larger discrepancies at lower temperatures. This range has led to considerable disagreement about the correct diffusivity and approach to apply to a given application. The observation of differences in H<sup>+</sup> loss profiles for different FTIR peaks (e.g., Tollar et al. 2015) is particularly important because if FTIR peaks must be resolved and analyzed individually, then H<sup>+</sup> data from secondary ion mass spectrometry (SIMS), a common and powerful technique, becomes significantly more difficult to interpret because SIMS measures only the total, or bulk, H<sup>+</sup>.

Bulk H<sup>+</sup> diffusion in natural olivine has been observed to occur at two different rates during hydration under pressure (Kohlstedt & Mackwell 1998; Demouchy & Mackwell 2006). The faster of these two rates was attributed to a flux of H<sup>+</sup> charge-balanced by a counter-flux of electrons. Because they distort the local lattice, these electrons are often called polarons, and so this “redox” rate has also sometimes been labeled proton-polaron (PP). The slower rate was attributed to a migration of metal vacancies parallel to the H<sup>+</sup> and so was referred to as the proton-vacancy (PV) rate. Neither of these studies note any significant differences between peaks, and subsequent work has generally assumed that dehydration proceeds similarly for bulk H<sup>+</sup>, first at the redox rate and then at the PV rate (Demouchy & Bolfan-Casanova 2016; Thoraval & Demouchy 2014).

Significant disagreement exists about which set of diffusivities to apply in a given situation.. For example, in studies of olivine phenocrysts, Le Voyer et al. (2014); Lloyd et al. (2013); and Hauri (2002) conclude that the redox rate applies, whereas Mironov et al. (2015); Portnyagin et al. (2008); Chen et al. (2011); and Gaetani et al. (2012) suggest using the PV rate. Xenolith studies face similar uncertainty,

with some studies mostly focusing on choosing between redox and PV rates (Demouchy et al. 2006; Peslier and Luhr 2006; Denis et al. 2013; Thoraval & Demouchy 2014) and others exploring peak-specific behavior and diffusivities (Hilchie et al. 2014; Tolan et al. 2015; Peslier et al. 2015)

The major goal of this work is to better understand which diffusivity to use for applications that involve H<sup>+</sup> diffusion in natural olivine. We focus our efforts mostly on dehydration, for which few experimental studies exist on natural Fe-bearing olivine despite the importance of this parameter for determining the ascent rate for xenoliths and phenocrysts.

## Methods

We provide, for the first time, time-series data showing H<sup>+</sup> loss from the same single crystal of Fe-bearing olivine. We carry out such a time series for two natural olivines: a partially hydrated xenolithic olivine from San Carlos and a phenocryst from Kilauea Iki. These data are coupled with independent estimates of the H<sup>+</sup> diffusivity based on H<sup>+</sup> zonation patterns in a second untreated Kilauea Iki phenocryst to produce a set of generic Arrhenius laws for H<sup>+</sup> diffusion in natural olivine with forsterite numbers between 86 and 90.

### *Sample selection*

Olivines from San Carlos, AZ and Kilauea Iki were chemically characterized and used for H<sup>+</sup> diffusion experiments. The San Carlos olivine was provided by David Kohlstedt and is similar to that used in previous hydration experiments (Mackwell and Kohlstedt 1990; Kohlstedt and Mackwell 1998). Here we extend that work by examining site-specific dehydration behavior. The Kilauea Iki olivines were collected from scoria from the 1959 Episode 1 eruption of Kilauea Iki and have been described in detail by David Ferguson (Ferguson et al. 2016), who provided the samples. The Kilauea Iki samples are of great interest because they provide the first direct experimental measurements of H<sup>+</sup> diffusion in all 3 crystallographic directions of inclusion-free olivine phenocrysts relevant to volcanic systems at low pressure, and, because independent estimates of the decompression rate already exist (Ferguson et al. 2016). We can also estimate the hydrogen diffusivity in the untreated olivine during its actual ascent.

### *Sample preparation*

A large crack- and inclusion-free piece of San Carlos olivine, SC1 (IGSN: IEFRSCO1), was oriented by Laue camera at Cornell University and then cut into a series of smaller pieces approximately 2-3 mm long on each side using a diamond saw. One of the resulting sub-pieces, SC1-1 (IGSN: IEFRJAI3), was polished with 0.25 μm diamond paste and used to estimate the initial H<sup>+</sup> concentration by FTIR. Additional pieces of SC1 were used to test the hydration procedure, and pieces SC1-7 (IGSN: IEFRJAI9) and SC1-2 (IGSN: IEFRJAI4) were partially hydrated and then polished with 0.25 μm diamond paste for FTIR. SC1-2 was then sequentially dehydrated with FTIR profiles measured after each dehydration step and afterwards analyzed by electron microprobe analysis (EMPA) and SIMS. Table 1 outlines the experimental treatment of each crystal piece.

Two large, relatively clear pieces of the Kilauea Iki olivine (Kiki) were selected, oriented based on crystal morphology, and polished. The orientation of both samples was confirmed by electron backscatter diffraction (EBSD) at the American Museum on Natural History. One of these samples, Kiki (IGSN: IEFRJAI), was polished into a block shape of dimensions 2 × 1 × 1.3 mm and characterized by EMPA, SIMS, and polarized FTIR. The sample was initially zoned in H<sup>+</sup>, and the low H<sup>+</sup> rims were polished off to create a homogeneous initial block for use in dehydration experiments.

This zonation was not polished off the second Kilauea Iki phenocryst (IGSN IEMN1KI02), which was used to obtain an independent estimate of the bulk H<sup>+</sup> diffusivity in olivine as degassing took place during ascent. This sample was polished to its midpoint to expose the (010) plane and prepared for SIMS

following recently developed sample preparation techniques for reducing instrumental background (Mosenfelder et al. 2011; Le Voyer et al. 2014; Newcombe et al. 2017). The phenocryst was cleaned in ultrasonic baths of toluene, acetone, and isopropanol; baked under vacuum at 110°C for ~72 hours; pressed into a 1-inch round aluminum mount containing indium metal; coated in Au; and allowed to degas in the sample exchange airlock for three days prior to analysis.

Sample thicknesses were measured with a digital micrometer accurate to within  $\pm 5 \mu\text{m}$ . Additional details for samples, including images and sample dimensions, are available online at [geosamples.org](http://geosamples.org).

### *Electron microprobe analysis*

Major elements of SC1-2 and Kiki were analyzed by electron microprobe at AMNH along traverses parallel to those on which H<sup>+</sup> measurements were made to confirm homogeneity of the samples. The beam current was 20 nA, and the accelerating voltage was 15 kV.

### *Initial H<sup>+</sup> concentrations by FTIR and NanoSIMS*

The initial H<sup>+</sup> concentration in each olivine used in dehydration experiments was estimated using both polarized FTIR and NanoSIMS. Polarized FTIR measurements were performed at AMNH using the Thermo Nicolet Nexus 670 infrared spectrometer and Thermo Nicolet Continuum 15× infrared microscope with a resolution of 4 cm<sup>-1</sup>, spot sizes of 100 × 100  $\mu\text{m}$ , an average of 200 scans, and a ZnSe polarizer. Initial H<sup>+</sup> concentrations were estimated from 3 orthogonal polarized measurements (Libowitzky and Rossman 1996; Shuai and Yang 2017) by applying the Bell and Withers calibrations (Bell et al. 2003; Withers et al. 2012). To account for the large error associated with baseline choice, 3 different baselines were drawn, and the resulting areas were averaged. Traverses along all three directions did not show significant zonation in bulk or peak-specific H<sup>+</sup> in the untreated samples.

Erik Hauri measured the C, H, F, P, and Cl concentrations by NanoSIMS along traverses parallel to *c* in SC1-2 and parallel to *b* in Kiki using calibrations similar to those for the SIMS analyses below. These NanoSIMS measurements were made before Kiki was dehydrated but after the final dehydration heating step for SC1-2. The area under the O-H stretching peaks with the electric vector E || *a* is equal to that of both the untreated SC1-1 ( $7 \pm 5 \text{ cm}^{-2}$ ) and of the partially hydrated and then dehydrated SC1-2 ( $7 \pm 6 \text{ cm}^{-2}$ ). Because the area is the same we assume that the final H concentration is roughly equal to the initial, and so the SIMS measurements of the hydrated and then dehydrated SC1-2 were taken as a reasonable estimate of the initial water concentration in SC1.

### *SIMS on untreated Kilauea Iki olivine*

Hydrogen profiles along the *a* and *c* crystallographic axes in the naturally zoned Kilauea Iki phenocryst were characterized by SIMS using the Cameca 6f-SIMS at the Department of Terrestrial Magnetism, Washington DC. Analyses were performed using a primary beam current of ~16 nA. The primary beam was rastered across a 35×35  $\mu\text{m}$  area during 300s of presputtering, and the area of the raster was reduced to 20×20  $\mu\text{m}$  during analysis. Use of a circular field aperture with a ~10- $\mu\text{m}$  diameter ensured that only ions from the central ~78  $\mu\text{m}^2$  of the analytical crater were collected. Counts of <sup>12</sup>C, <sup>16</sup>O<sup>1</sup>H, <sup>19</sup>F, <sup>30</sup>Si, <sup>31</sup>P, <sup>32</sup>S, and <sup>35</sup>Cl were detected by an electron multiplier. A linear relationship between <sup>16</sup>O<sup>1</sup>H/<sup>30</sup>Si and H<sup>+</sup> concentration was defined by measurements of olivine and orthopyroxene standards (Koga et al. 2003). MEGAN: Please insert the actual numbers for the calibration here. Background counts of <sup>16</sup>O<sup>1</sup>H were assessed via frequent analysis of nominally dry Suprasil 3002 silica glass (purchased from Heraeus Quarzglas, Switzerland). Replicate analyses of Suprasil glass indicate that the detection limit of our water analyses was 1.5 ppm H<sub>2</sub>O following the methodology of Long and Winefordner 1983. Analytical drift throughout the session was monitored via frequent analysis of Herasil 102 silica glass (purchased from Heraeus) containing ~55 ppm H<sub>2</sub>O.

### *Hydration of San Carlos olivine*

Two pieces of previously oriented San Carlos olivine SC1, SC1-2 and SC1-7, were partially hydrated in a  $\frac{3}{4}$ " Boyd-type piston cylinder apparatus with a BaCO<sub>3</sub> pressure medium using a procedure broadly similar to that of Jollands et al. (2016). Here the samples were placed in copper capsules and surrounded by liquid distilled H<sub>2</sub>O and a powdered mixture of Ni and NiO to control oxygen fugacity and San Carlos olivine and enstatite to control silica activity (Figure 1). Temperatures were controlled with a D-type thermocouple (W3%Re-W25%Re) with control precision of  $\pm 2^\circ\text{C}$  and probable accuracy of  $\pm 20^\circ\text{C}$ . After rapid quenching followed by relatively slow decompression, the capsules were pierced with a drill to confirm water was still present and then dissolved overnight in a mixture of 1:1 H<sub>2</sub>O to HNO<sub>3</sub>. The rectangular parallelepiped samples were then mounted in CrystalBond, polished with 0.25  $\mu\text{m}$  diamond paste on all sides, and cleaned in acetone.

SC1-2 was hydrated at a nominal temperature of 800°C and 10 kbar pressure, which corresponds to a water fugacity of 1.6 GPa (Withers 2013), for 17.5 hours. That time was chosen in order to reach, but not pass, what Kohlstedt and Mackwell (1998) call "metastable equilibrium". If the model used by Kohlstedt and Mackwell (1998) is correct, the H<sup>+</sup> concentration in SC1-2 after the piston cylinder experiment should be homogeneous, and the concentration should be lower than the true solubility and presumably determined by the initial concentration of ferric iron. If the metastable equilibrium H<sup>+</sup> concentration is both large enough to easily measure and homogeneous, then SC1-2 is a suitable starting material for step-wise dehydration experiments.

SC1-7 was heated for 7 hours at 10 kbar and temperature readings of 1000°C, but the experiment ended when capsule began to melt, suggesting the true temperature in the capsule was closer to 1085°C, the melting point of copper or, more likely, the Cu was contaminated, perhaps with a small amount of oxygen, resulting in freezing point depression. This temperature range and pressure correspond to water fugacities of 1.9-2.0 GPa (Withers 2013). Within this temperature range, given the dimensions of the sample and the diffusivities reported by Kohlstedt and Mackwell (1998), the experiment time of 7 hours should allow the completion of redox-rate diffusion and initiation of diffusion at the slower PV rate without fully saturating the sample. This experiment allows a direct comparison with previous work (Kohlstedt and Mackwell 1998; Demouchy and Mackwell 2006).

### *Dehydration*

Olivine samples SC1-2 (the same sample that was partially hydrated according to the procedure described above) and Kiki (untreated) were dehydrated in increments using the vertical furnace used in previous dehydration experiments (Ferriss 2015), and oxygen fugacity was controlled with a mixture of CO and CO<sub>2</sub>. The partially hydrated sample SC1-2 was heated at 800°C for 1, 3, 7, 13, 19, 43, and 68 hours at an oxygen fugacity  $10^{-16.5}$  bars, equivalent to NNO-2.6, where NNO is the nickel-nickel oxide buffer. Kiki was heated at 800°C for 1 and 8 hours; then 3, 6, 7, and 8 hours at 1000°C. All heating steps for Kiki were conducted at oxygen fugacity of NNO-2.6 except for the final step at 1000°C, which was conducted at relatively oxidizing conditions, NNO+2. The low fO<sub>2</sub> at which most of the dehydration steps were carried out was unintentional. A summary of all experimental run conditions is provided in Table 1.

### *FTIR Analyses of Treated Samples*

Before heat treatment and in between each heating step, samples were analyzed by polarized FTIR along 3 orthogonal traverses parallel to the three crystallographic directions in the uncut crystal (Figure 2). These analyses use the same conditions described above for estimating the initial water and were in all cases conducted with polarized radiation with the electric vector E || *a* to provide a consistent set of measurements for each direction with high areas under the O-H stretching peaks (Figure 3). Quadratic baselines were drawn based on the curve of the spectrum of the untreated and/or the dehydrated sample, with typical wavenumber ranges of 3200-3700 cm<sup>-1</sup>. Each profile was normalized to the initial

measurements to produce a ratio of the final to initial area  $A/A_0$  and scaled up to a true concentration based on the initial concentrations,  $A_0$ , determined above. These “whole-block” concentrations represent the average concentration through the entire path of the infrared beam and could be used to determine diffusivities in all three crystallographic directions following the fitting procedure described below (after Ferriss et al., 2015).

To explore possible differences among various  $H^+$  defects, the same normalization and fitting procedures were applied to individual peaks using the peak heights relative to the quadratic baseline. Particular emphasis was placed on peaks at the following 4 wavenumbers: 3600, 3525, 3356, and 3236  $\text{cm}^{-1}$ . The peak at  $3600 \text{ cm}^{-1}$ , designated [Si-4H], is most likely  $4H^+$  in a  $\text{Si}^{4+}$  vacancy with a nearby  $\text{Fe}^{2+}$  (Blanchard et al. 2017). The peak at  $3525 \text{ cm}^{-1}$ , designated [Ti-2H], is one of two prominent peaks produced by  $2H^+$  coupled with a  $\text{Si}^{4+}$  vacancy and a  $\text{Ti}^{4+}$  on a metal site. We focus on this peak both to minimize interference with nearby [Si-4H] peaks and to more directly compare with the results of Padrón-Navarta, Hermann, and O’Neill (2014). The  $3356 \text{ cm}^{-1}$  peak, designated [tri-H], is the most prominent peak in a doublet associated with a  $\text{Mg}^{2+}$  vacancy charge-balanced by  $H^+$  and  $\text{Fe}^{3+}$  substituting on a metal site (Blanchard et al. 2017), and the  $3236 \text{ cm}^{-1}$  peak, designated [Mg-2H], is likely  $2H^+$  charge-balanced by a  $\text{Mg}^{2+}$  vacancy (Berry et al. 2005).

All of the raw FTIR spectra, baselines, and computer code used to produce all calculations and figures reported in this paper will be made available on GitHub.

Table 1. Experimental conditions for San Carlos olivine samples SC1-7 and SC1-2 and Kilauea Iki olivine Kiki

Sample name	Temperature (Celsius)	Pressure (GPa)	fO <sub>2</sub> Buffer	log fO <sub>2</sub> in bars	Heating time (hours)	Total dehydration time at constant temperature (hours)
SC1-7	1000	1	NNO	-10.3	7	-
SC1-2	800	1	NNO	-13.9	17.4	-
SC1-2	800	0.0001	NNO – 2.6	-16.5	1	1
SC1-2	800	0.0001	NNO – 2.6	-16.5	2	3
SC1-2	800	0.0001	NNO – 2.6	-16.5	4	7
SC1-2	800	0.0001	NNO – 2.6	-16.5	6	13
SC1-2	800	0.0001	NNO – 2.6	-16.5	6	19
SC1-2	800	0.0001	NNO – 2.6	-16.5	24	43
SC1-2	800	0.0001	NNO – 2.6	-16.5	25	68
Kiki	800	0.0001	NNO – 2.6	-16.5	1	1
Kiki	800	0.0001	NNO – 2.6	-16.5	7	8
Kiki	1000	0.0001	NNO – 2.6	-13.1	3	3
Kiki	1000	0.0001	NNO – 2.6	-13.1	3	6
Kiki	1000	0.0001	NNO – 2.6	-13.1	1	7
Kiki	1000	0.0001	NNO + 1.9	-8.4	1	8

### *Diffusion modeling*

$H^+$  diffusivities in each direction were obtained from the whole-block FTIR data after each time step using forward models modified to account for path integration effects. The 3-dimensional internal concentration,  $v$ , is calculated from the time  $t$  and diffusivities  $D$  in each direction for a rectangular parallelepiped with unit initial concentration and zero external concentration for the region  $0 < x < L_a$ ,  $0 < y < L_b$ ;  $0 < z < L_c$  as follows (Carslaw and Jaeger 1959):

Eq1

$$v = \left( \operatorname{erf} \left( \frac{x}{2\sqrt{D_a t}} \right) + \operatorname{erf} \left( \frac{L_a - x}{2\sqrt{D_a t}} \right) \right) \times \left( \operatorname{erf} \left( \frac{y}{2\sqrt{D_b t}} \right) + \operatorname{erf} \left( \frac{L_b - y}{2\sqrt{D_b t}} \right) \right) \times \left( \operatorname{erf} \left( \frac{z}{2\sqrt{D_c t}} \right) + \operatorname{erf} \left( \frac{L_c - z}{2\sqrt{D_c t}} \right) \right)$$

The internal concentrations are then averaged along the ray path of the FTIR observations to obtain path-integrated profiles. These “whole-block” profiles are then fit to the data measured in the uncut block. These models are described in more detail by E. Ferriss et al. (2015) and implemented using the free, open-source software package pynams (Ferriss 2015).

For the SIMS profiles of the zoned Kilauea Iki phenocryst, we estimated the diffusivity using a Monte Carlo model of diffusive  $H^+$  loss from the olivine phenocryst in response to syneruptive degassing of its host magma. We assume an average decompression rate of  $0.05 \pm 0.005$  MPa/s from Ferguson et al. 2016 based on the diffusive loss of volatiles from olivine-hosted melt embayments from the same group of samples (Ferguson et al. 2016) and that the volatile concentration of the host magma follows a closed-system degassing path (Witham et al. 2012). We use a 1-dimensional (1D) finite element model, which is appropriate if a central concentration plateau is observed, which would suggest that  $H^+$  diffusion has not reached the center of the crystal (Thoraval and Demouchy 2014, Shea et al. 2015). The concentration of  $H^+$  dissolved in olivine in equilibrium with the degassing magma (i.e., the boundary condition at the exterior edge of the crystal) is calculated at each time step with a partition coefficient  $K_d$ . The diffusivity of  $H^+$ , the magma decompression rate ( $dP/dt$ ), and the partition coefficient are treated as free parameters in the model. Best-fit values of these parameters were determined via least-squares fitting to 100 synthetic water concentration profiles generated by assuming each  $H^+$  concentration measurement is normally distributed with a mean corresponding to the measured value and a standard deviation of 0.35 ppm  $H_2O$ . The least-squares minimization was performed using the ‘fminsearch’ MATLAB function. Starting values of  $D$ ,  $dP/dt$ , and  $K_d$  were drawn at random from the following uniform distributions spanning suitable ranges:  $-9.5 < \log D$  ( $m^2/s$ )  $< -10.5$ ;  $0.045 < dP/dt$  (MPa/s)  $< 0.055$ ; and  $0.0012 < K_d < 0.0017$ .

## Results

### *Characterization of the starting material*

Microprobe analysis did not reveal any significant zonation along the measured profiles and were generally consistent with previous work (Ruprecht and Plank 2013; Ferguson et al. 2016) with somewhat lower forsterite numbers:  $87.7 \pm 0.2$  in SC1-2 and  $86.2 \pm 0.2$  in Kiki (detailed traverse information and standard measurements are in the Supplemental Tables). The San Carlos olivine used in previous  $H^+$  diffusion experiments had a reported approximate composition with forsterite number 91 (Mackwell and Kohlstedt 1990). This large difference in forsterite content suggests that the San Carlos olivine that we are using came from a different xenolith than the samples used in previous work. The initial water concentration was estimated from the polarized FTIR measurements and baselines shown in Figure 3 using both the Bell calibration and the Withers calibration and also by nanoSIMS (Table 2). These three estimates were averaged to produce initial  $H^+$  concentration estimates of  $15 \pm 2$  ppm  $H_2O$  in the Kilauea Iki olivine and  $4 \pm 1$  ppm  $H_2O$  in the San Carlos olivine. These low concentrations are consistent with

previous work on San Carlos olivine (Peslier and Luhr 2006; Kurosawa, Yurimoto, and Sueno 1997) Gaetani et al., 2014. The H<sup>+</sup> concentration in the Kilauea Iki sample, for which the low rims had been polished off to prepare the sample as a rectangular parallelepiped, was homogeneous by both SIMS and FTIR.

Several different O-H absorption peaks were observed in FTIR profiles of the initial materials. The prominent peaks at wavenumbers 3525 and 3573 cm<sup>-1</sup> oriented primarily ||  $\alpha$  in both Kilauea Iki and San Carlos olivine correspond to the [Ti-2H] incorporation mechanism, and the high-wavenumber peaks that primarily appear as shoulders on the [Ti-2H] peaks correspond to [Si-4H] (Berry et al. 2005). A very small peak at 3600 cm<sup>-1</sup> present in both samples has been ascribed to [Si-4H] with nearby Fe<sup>2+</sup> (Blanchard et al. 2017).[Si-4H] The Kilauea Iki olivine, but not the untreated San Carlos olivine, contains prominent [tri-H] peaks. These peaks at 3356 and 3329 cm<sup>-1</sup> correspond exactly to the peak locations that Blanchard et al. (2017) associate with Fe<sup>3+</sup>[tri-H]. No [Mg-2H] peaks were present initially in these spectra with E ||  $\alpha$ .

Table 2. H<sup>+</sup> concentration estimates for Kilauea Iki olivine and San Carlos olivine based on polarized FTIR areas (Figure 3) and SIMS measurements.

	Kilauea Iki olivine; Kiki	San Carlos olivine; sub-samples of SC1	
FTIR area E    $\alpha$ (cm <sup>-2</sup> )	52+-10	7+-5	untreated SC1-1
		55+-17	partially hydrated SC1-7
		24+-8	partially hydrated SC1-2
		7+-6	dehydrated SC1-2
FTIR area E    b (cm <sup>-2</sup> )	31+-13	8+-5	untreated SC1-1
FTIR area E    c (cm <sup>-2</sup> )	18+-9	9+-4	untreated SC1-1
FTIR area summed over 3 directions (cm <sup>-2</sup> )	101+-19	24+-8	untreated SC1-1
Water, Bell calibration (ppm H <sub>2</sub> O)	19+-4	4.5+-1.5	untreated SC1-1
Water, Withers calibration (ppm H <sub>2</sub> O)	12+-2	3+-1	untreated SC1-1
Water, SIMS (ppm H <sub>2</sub> O)	14+-1	5+-1	dehydrated SC1-2
Average initial water (ppm H <sub>2</sub> O)	15+-2	4+-1	SC1
Ratio of water in ppm H <sub>2</sub> O to area in cm <sup>-2</sup> with E    $\alpha$	0.3	0.6	SC1-1
Average water (ppm H <sub>2</sub> O) after piston cylinder experiment	Not treated with pressure	32+-23 14+-10	partially hydrated SC1-7 partially hydrated SC1-2

### Hydration

Changes in FTIR absorbance indicate that H<sup>+</sup> was successfully incorporated into San Carlos olivine samples SC1-7 and SC1-2 (Figure 4A). To construct H<sup>+</sup> profiles, quadratic baselines were drawn to match both the curve of the spectrum of the untreated sample and the middle baselines used to determine the initial water concentration in Figure 3. Typical baselines are illustrated in Figure 4B and C, and all spectra and baselines are shown in the Supplement. The area under each curve was determined and scaled to an estimated H<sup>+</sup> concentration by multiplying by 0.6, following the ratio of concentration to area with E ||  $\alpha$  reported for San Carlos olivine in Table 2.

The partially hydrated sample SC1-2 was sufficiently homogeneous for both bulk H<sup>+</sup> and individual peaks to serve as a reasonable starting material for subsequent dehydration experiments (Figure 4). If we ignore the uncertainties associated with baseline choice and use only the quadratic baseline shown in Figure 4C, the H<sup>+</sup> concentration across hydrated SC1-2 is 15±1 ppm H<sub>2</sub>O. Although there is a small

increase in area around the [tri-H] peaks, the large majority of the H<sup>+</sup> in the hydrated SC1-2 is present as [Ti-2H] and [Si-4H], and these profiles are also homogeneous. This crystal was hydrated long enough to achieve the “metastable equilibrium” of Kohlstedt and Mackwell (1998). The homogeneous concentration across the crystal and its rapid rate of hydration are consistent with Kohlstedt and Mackwell’s experiments.

In contrast, H<sup>+</sup> zonation is clearly observed in SC1-7, which was hydrated longer (Table 1), with central water concentrations of 38±7 ppm H<sub>2</sub>O (using the quadratic baseline shown in Figure 4B). The intent was to enter the slower, PV stage of hydration. The variations in concentration are most apparent || c for bulk H and all major peaks (Figure 5), consistent with previously work showing c is the fast direction during PV rate diffusion (Kohlstedt and Mackwell 1998; Demouchy and Mackwell 2006).

Quantifying the diffusivities in SC1-7 requires assumptions about both the solubility and metastable equilibrium concentrations. Here we assume a metastable equilibrium concentration of 15±1 ppm H<sub>2</sub>O, the observed concentration in SC1-2. This value is much higher than the 0.4 ppm H<sub>2</sub>O (7 H/10<sup>6</sup>Si) reported by Kohlstedt and Mackwell (1998). This large difference has been difficult to reconcile but may be related in part to differences in the forsterite content and/or the calibrations used to determine H<sup>+</sup> concentrations from FTIR spectra in the two studies. The accepted values for the PV rate (Demouchy and Mackwell 2006) fit our data reasonably well if we assume a final solubility of 150 ppm H<sub>2</sub>O, which is possible, particularly given the still large uncertainties in the solubility of H<sup>+</sup> in olivine (Tollan et al. 2017:20; Zhao, Ginsberg, and Kohlstedt 2004; Mosenfelder et al. 2006). Figure 5 shows the best fit to our whole-block SC1-7 data that assumes a final concentration equal to the maximum observed concentration of 58 ppm H<sub>2</sub>O. This fit requires higher diffusivities than Demouchy and Mackwell’s (2006) PV diffusivities, particularly || b. Diffusivities higher along b than c are unexpected but not entirely without precedent (e.g., Demouchy et al. 2016; Demouchy and Mackwell 2003) and not well constrained here by three interior points.

### *Dehydration*

SC1-2 and Kiki, two homogeneous blocks of olivine with similar initial starting H<sup>+</sup> concentrations but very different histories, compositions, and distributions of H<sup>+</sup>, were sequentially dehydrated in a gas-mixing furnace (Figure 6). The choice of baseline is well known as a major source of error in FTIR analyses, and associated errors in the resulting peak heights and areas may be as high as 30%, consistent across profiles. All profiles were normalized to a relatively homogeneous starting profile. While this error due to baseline selection is very large, it is a consistent offset for all estimates that is mostly eliminated by dividing by the initial values, which contain the same systemic error related to baseline choice.

Path-integrated 3-dimensional diffusion modeling was then performed on each profile to estimate the rate of H<sup>+</sup> movement after each heating step and associated errors (see Supplemental PDF). These efforts are described in more detail for each sample in the sections below. Most of the resulting diffusivities (see Supplemental Table) show H<sup>+</sup> loss rates that are *intermediate* between the redox and PV rates.

### *Dehydration of San Carlos olivine*

We determined H<sup>+</sup> loss curves and diffusivities for bulk H<sup>+</sup>, [Si-4H] at 3600 cm<sup>-1</sup>, and [Ti-2H] at 3525 cm<sup>-1</sup> in San Carlos SC1-2. All spectra, baselines, profile data, and best-fit curves are provided in the Supplemental PDF. Selected profile data are shown in comparison with expected redox rate profiles in Figure 7, and all estimated diffusivities are shown as a function of heating time in Figure 8.

The height of the [Si-4H] peak clearly decreases more slowly than the rest of the peaks and did not decrease in height during the first 5 heating steps at 800°C. After 43 hours, when the large majority of the initial H<sup>+</sup> had left the crystal and the bulk of the remaining H<sup>+</sup> was present in the [Si-4H peak], clear

$H^+$ -loss profiles could be observed for [Si-4H], with apparent diffusivities that were relatively fast compared to the initial stages and with a fast direction  $\parallel a$ . These [Si-4H] loss profiles also differ from the majority of profiles observed in this study in that they did not decrease to zero near the edges, but rather to about 40% of the initial concentration, which was the final concentration used when modeling the diffusivities. Over the course of the final heating steps, the rate of [Si-4H] movement increased noticeably, from  $10^{-12.6} \text{ m}^2/\text{s}$  at 19 hours to  $10^{-11.8} \text{ m}^2/\text{s} \parallel a$  at 68 hours.

While the decrease in the height of the [Si-4H] peak accelerated during the experiment, the loss of  $H^+$  from the [Ti-2H] peak slowed down. To observe this decrease in  $H^+$  loss rate in the profile data, compare the close correspondence of the [Ti-2H] data with the expected redox rate curves at 7 hours with the large difference between the data and the redox curves at 19 hours (Figure 7D-F). The [Si-4H] and [Ti-2H] diffusivities eventually come close to converging, but the [Ti-2H] peak diffusivity is always higher (Figure 8). Profiles for the other [Ti-2H] peak and additional [Si-4H] peaks in SC1-2 are not shown but behave similarly to [Ti-2H].

The bulk  $H^+$  curves, which consist of a combination of peaks, the [Si-4H] and [Ti-2H] peaks, show apparent diffusivities that are intermediate between the final [Ti-2H] and [Si-4H] mechanism diffusivities. The bulk  $H^+$  curves are typically less symmetric than the profiles of either the [Ti-2H] or [Si-4H] peak, in part because of the occasional appearance of spectra with relatively large [tri-H] peaks and distorted baselines (see Supplemental PDF, e.g., 100  $\mu\text{m}$  from the edge along  $a$  after 43 hours of heat treatment). This [tri-H] appeared intermittently near all edges of SC1-2 frequently enough that it is unlikely to be contamination but too infrequently to model with confidence. The final bulk  $H^+$  concentration was modeled using 15% of the initial homogeneous partially hydrated concentration because the [Si-4H] peak does not decrease to zero at the rim (as noted above), and therefore the bulk  $H^+$  also cannot go to zero. During initial dehydration stages, when the [Si-4H] peak at  $3600 \text{ cm}^{-1}$  was a relatively minor component, the bulk  $H^+$  could be modeled well with redox, similar to [Ti-2H]. By the end of the experiment, the bulk  $H^+$  diffusivity had dropped from  $10^{-10.9} \text{ m}^2/\text{s} \parallel a$ .

### Experimental dehydration of Kilauea Iki olivine

Experimentation on the Kilauea Iki sample took place in two stages. First, the sample was treated exactly the same way as SC1-2 during dehydration: heated at  $800^\circ\text{C}$  in a gas-mixing furnace at NNO-2.6. Second, the sample was sequentially heated at  $1000^\circ\text{C}$ , largely at NNO-2.6 (for 3, 6 and 7 total hrs) and then at NNO+1.9 for a final increment at 8 total hours. Heating the Kilauea Iki sample at  $800^\circ\text{C}$  for 8 hours did not produce any clear loss in bulk H or [Ti-2H] (Figure 9). Although bulk  $H^+$  and [Ti-2H] did not change, heating the Kilauea Iki olivine at  $800^\circ\text{C}$  did result in significant re-organization, where the  $H^+$  from [tri-H] decreased by 50% and the H from [Si-4H] doubled. The Kilauea Iki  $800^\circ\text{C}$  [tri-H] loss on reorganization rates were initially fast, around  $10^{-11.0} \text{ m}^2/\text{s} \parallel c$  at 1 hour before dropping to  $10^{-12.5} \text{ m}^2/\text{s}$  at 8 hours. This drop in the [tri-H] movement rate suggests that the large majority of the internal  $H^+$  reorganization had been completed. The relative flatness of all of the profiles suggests that the movement was occurring everywhere throughout the crystal simultaneously, consistent with reorganization. The profiles from these 8 hours of heating at  $800^\circ\text{C}$  were used as the ‘initial’ profiles for data collected during a second stage of heating at a higher temperature.

The heating temperature was raised to  $1000^\circ\text{C}$  because the maximum bulk  $H^+$  diffusivities observed at  $800^\circ\text{C}$  were unlikely to produce clear  $H^+$  loss profiles within laboratory time scales. The oxygen fugacity was maintained along the same buffer curve, NNO-2.6, for 3 heating steps totaling 3, 6, and 7 hours, and in each of these steps, the rate of  $H^+$  loss could be estimated as  $10^{-10.9} \text{ m}^2/\text{s}$  for bulk  $H^+$  and [Ti-2H] and  $10^{-10.7} \text{ m}^2/\text{s}$  for [Si-4H] parallel to the fast direction  $a$ . These fits are shown in Figure 10 for the 6 hour data, and the rest are provided in the Supplement. The [Si-4H] loss profiles in Kilauea Iki (Figure 10 J-L), unlike in San Carlos (Figure 7G-I), appear to decrease to zero concentration at the rim, and to

decrease at a rate faster than [Ti-2H]. The [tri-H] loss at 1000°C was slower than the other peaks and did not include an obvious fast direction.

A final heating step of 1 additional hour was performed for a total of 8 hours heating at 1000°C under more oxidizing conditions, NNO+1.9. The resulting loss of H<sup>+</sup> for all mechanisms was consistent with the diffusivities determined under more reducing conditions, which suggests that the role of oxygen fugacity has little effect on the diffusivities, at least for this very late stage of dehydration and over such short timescales (1 hour).

### *Bulk H<sup>+</sup> diffusivity in Kilauea Iki olivine during ascent*

SIMS analysis of a natural Kilauea Iki olivine phenocryst along its crystallographic *a* axis indicates a central H<sup>+</sup> concentration of ~11 ppm H<sub>2</sub>O, decreasing to concentrations of ~6 ppm at the crystal edges (Figure 11). The H<sup>+</sup> concentration gradients recorded in the outer ~200 μm of the crystal are suggestive of syneruptive water loss from the olivine in response to degassing of the host magma on ascent. Unlike the profile along *a*, the profile measured along *c* exhibits a constant H<sup>+</sup> concentration. No decrease in H<sup>+</sup> concentration was detected at the edge of the crystal along the *c* axis, suggesting that any signature of syneruptive degassing along the *c* direction may be confined to the region <~20 μm from the edge of the crystal, i.e., not resolvable at the spatial resolution of our analyses. These observations thus indicate that this crystal experienced greater loss of H<sup>+</sup> parallel to *a* than parallel to *c*.

The plateau in H<sup>+</sup> concentration along *a* (the apparent fast direction) supports our use of a 1D model, the results of which indicate a trade-off between D and K<sub>d</sub>, with higher best-fit values of K<sub>d</sub> resulting in higher best-fit values of D. No clear trade-off is observed between best-fit values of D and dP/dt. Our Monte-Carlo simulation suggests a H<sup>+</sup> diffusivity || *a* of  $10^{-10.17 \pm 0.08}$  m<sup>2</sup>/s at the temperature 1200°C determined by Ferguson et al. 2016.

### *Estimated bulk H diffusivity during dehydration of natural olivine*

Although the treated crystals show some complex phenomena, such as rapid reorganization of peaks and rate changes with time, we use the H<sup>+</sup> diffusivities determined at the end of each experiment, (i.e., the data in San Carlos olivine SC1-2 after 68 hours of heating at 800°C and in the Kilauea Iki olivine after 8 hours of heating at 1000°C) combined with the diffusivity || *a* for the untreated Kilauea Iki olivine at 1200°C, to estimate common Arrhenius laws for bulk H<sup>+</sup> in natural Fe-bearing olivine in all three directions during dehydration (Figure 12). For convenience, we assume a constant activation energy of 130 kJ/mol and vary the pre-exponential factor D<sub>0</sub>, which, as plotted in Figure 12, is  $10^{-5.4}$  m<sup>2</sup>/s || *a*,  $10^{-6.9}$  m<sup>2</sup>/s || *b*, and  $10^{-6.6}$  m<sup>2</sup>/s || *c*. The errors on these estimates are difficult to estimate with only 2 to 3 data points, and additional data, particularly at high temperatures, would be very useful. The final diffusivity estimates for [Ti-2H] and [Si-4H] are similar to those for bulk H<sup>+</sup> and so are likely to follow similar Arrhenius laws.

## Discussion

### *Overview of changes in the defect structures*

Our results suggest that in addition to driving H<sup>+</sup> in or out of the structure, the stability of a hydrated olivine may in some cases be increased by a redistribution of the H<sup>+</sup> among different sites. H redistribution can be seen in both the San Carlos olivine (i.e., the coupled slowing down of the rate of [Ti-2H] loss with the speeding up of [Si-4H] loss) and Kilauea Iki olivine (i.e., the coupled increase in [Si-4H] with decrease in [tri-H]). Table 3 provides an overview of the defects involved in these reactions. For this discussion, we follow Kohlstedt and Mackwell 1998 by writing the incorporated H<sup>+</sup> as a hydroxyl,

OH, on an O site and grouping defect associates in curly braces when using Kröger-Vink notation, which is described in the introduction.

Table 3. List of defects in discussion

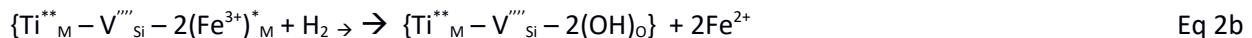
Defect label	Kröger-Vink notation	Olivine formula	FTIR peak location (cm <sup>-1</sup> )
[Ti-2H]	{Ti <sup>**</sup> <sub>M</sub> - V <sup>'''</sup> <sub>Si</sub> - 2(OH) <sub>O</sub> }	MgTiH <sub>2</sub> O <sub>4</sub>	3525, 3573
[Ti-2Fe <sup>3+</sup> ]	{Ti <sup>**</sup> <sub>M</sub> - V <sup>'''</sup> <sub>Si</sub> - 2(Fe <sup>3+</sup> ) <sup>*</sup> <sub>M</sub> }	MgTiFe <sub>2</sub> SiO <sub>8</sub>	None
[Si-4H]	{V <sup>'''</sup> <sub>Si</sub> - 4(OH) <sup>*</sup> <sub>O</sub> }	Mg <sub>2</sub> H <sub>4</sub> O <sub>4</sub>	3600
[Si-2H]	{V <sup>'''</sup> <sub>Si</sub> - 2(Fe <sup>3+</sup> ) <sup>*</sup> <sub>M</sub> - 2(OH) <sup>*</sup> <sub>O</sub> }	Fe <sub>2</sub> H <sub>2</sub> O <sub>4</sub>	3600
[Si-4Fe <sup>3+</sup> ]	{V <sup>'''</sup> <sub>Si</sub> - 4(Fe <sup>3+</sup> ) <sup>*</sup> <sub>M</sub> }	Fe <sub>4</sub> SiO <sub>8</sub>	None
[tri-H]	{V <sup>''</sup> <sub>M</sub> - (Fe <sup>3+</sup> ) <sub>M</sub> - (OH) <sup>*</sup> <sub>O</sub> }	FeHSiO <sub>4</sub>	3356
[tri-2Fe <sup>3+</sup> ]	{V <sup>''</sup> <sub>M</sub> - 2(Fe <sup>3+</sup> ) <sup>*</sup> <sub>M</sub> }	MgFe <sub>2</sub> Si <sub>2</sub> O <sub>8</sub>	None

### Defect evolution during hydration and dehydration San Carlos olivine

Figure 13 illustrates the inferred evolution of H-defects during hydration and then dehydration of our single block of San Carlos olivine, SC1-2. Panels 13A to 13B show rapid hydration, which affected primarily [Ti-2H] and occurred at the redox rate, with the fast direction ||  $a$ . The fact that H<sup>+</sup> was able to enter San Carlos olivine so quickly in the first hours of hydration at the redox rate suggests the movement of protons and electrons only. The diffusion of metals or vacancies is too slow to accommodate this rapid hydration. This means that the defect structure must have already been favorable to a redox mechanism of hydration. Given that [Ti-2H] was the dominant defect that was formed at the redox rate, the likely initial defect structure must have included Ti already present in the octahedral site with nearby Fe<sup>3+</sup> to create charge balance with the associated Si vacancy. Such [Ti-Fe<sup>3+</sup>] defects are primed for rapid hydration, with 2H supplying the electrons needed to reduce the 2Fe<sup>3+</sup> to 2Fe<sup>2+</sup>, forming protons that then create [Ti-2H]. This reaction may be described broadly for hydration (Figure 13 A → B) as



In Kröger-Vink notation as



and in terms of olivine formula units as



As discussed in Padron-Navarta (2014), Ti may also be present in the tetrahedral site, but such Ti will not be able to move to the octahedral site and form [Ti-2H] in hours. Instead, the presence of octahedral Ti in San Carlos olivine may be explained by slow hydration incorporation reactions that require octahedral Ti occurring at high temperature (e.g., the reverse of the reaction described by Padron-Navarta et al. 2014 Eq 3b). This Ti is then locked into the octahedral site during rapid dehydration and cooling over hours in a lava flow. The geological occurrence of our San Carlos olivine is

unknown in detail, but likely derives from one of the large xenoliths hosted in San Carlos lavas. Such rapid cooling would have exploited the same kind of redox mechanism in moving from 13A to 13B, but in reverse. Thus, any rapid influx of H<sup>+</sup> at the redox rate into an olivine may be limited not only by the initial quantity of Fe<sup>3+</sup> (Kohlstedt and Mackwell 1998) but the initial amount of octahedral Ti. Such a process is sometimes referred to as rapid “decoration” of existing defects. In this case, the initial defects were created by cooling in a lava flow.

Panels 13B to 13C illustrate the initial, rapid dehydration of the same San Carlos SC1-2 block that had just been hydrated rapidly. The initial dehydration was manifest entirely in a decrease in the [Ti-2H] peak, once again at the redox rate, with a fast direction ||  $\alpha$  (Figure 7D). This dehydration can be viewed as a reversal of the redox-mediated hydration that had just occurred (which was itself a reversal of redox-mediated dehydration that had occurred in nature, in the lava). The [Ti-2H] defects that had just formed were favorable for rapid dehydration, as 2H<sup>+</sup> gained electrons from nearby Fe<sup>2+</sup>, oxidizing the Fe<sup>3+</sup> once again, and potentially moving rapidly through the lattice again as neutral H<sub>2</sub>. The reactions can be written as Eq2a-c in reverse. Most of the [Si-4H] peaks behaved similarly to [Ti-2H], with the exception of one small peak at 3600 cm<sup>-1</sup> (Figure 6). The increase in the rate of this [Si-4H] peak at 3600 cm<sup>-1</sup> movement coupled with a decrease in the rate of [Ti-2H] (Figure 8) suggests that at least some of the H<sup>+</sup> leaving the [Si-4H] is doing so by moving into other Si vacancies associated with [Ti-2H] rather than leaving the crystal directly (Figure 13).

After 19 hours, the [Si-4H] peak at 3600 cm<sup>-1</sup> also started to drop, as the rate of decrease in the [Ti-2H] peak slowed (Figure 8). The coupled rate changes in these peaks suggest that at least some of the H<sup>+</sup> leaving [Si-4H] is doing so by moving into Si vacancies associated with [Ti-2H] rather than leaving the crystal directly. Panels 13C to 13D illustrate this reorganization of H<sup>+</sup>, moving from [Si-4H] to [Ti-2H] (Figure 13). The [Ti-2H] mechanism is known from incorporation studies as a particularly favorable position for H<sup>+</sup> (e.g., Berry et al. 2005). Because of the relative stability of [Ti-2H], any H<sup>+</sup> that is unable to leave readily by redox from [Si-4H] may prefer to move into recently-vacated Si vacancies that bring it closer to the octahedral Ti. This redistribution of H<sup>+</sup> between sites may be described broadly as



or, for partial dehydration of the [Si-4H] when only one [Ti-2Fe<sup>3+</sup>] defect is available (Figure 13 C → D):



Eq 4 may be described in Kröger-Vink notation as



and in terms of olivine formula units as



The coupling of H<sup>+</sup> loss from [Ti-2H] with its gain from [Si-4H] may explain both the observed change in apparent diffusivities (Figure 8) and the possibility of buffering or reaching a steady state in the overall rate of bulk H<sup>+</sup> loss., which may be set by the rate at which H<sup>+</sup> redistributes between [Si-4H] and [Ti-2H]. The H<sup>+</sup> leaves quickly from [Ti-2H] at the redox rate throughout the duration of the experiment, but the peak appears to slow down as more and more H<sup>+</sup> moves into [Ti-2H] from [Si-4H]. Thus, the observed

loss of the [Si-4H] peak may not represent H<sup>+</sup> moving out of the sample at all, but rather may indicate the rate at which the H<sup>+</sup> is redistributing between sites. As the slower rate, the redistribution rate between [Si-4H] and [Ti-2H] may set the bulk loss of H<sup>+</sup> from the San Carlos. This redistribution is slow enough to observe over a period of days because this experiment was conducted at the relatively low temperature of 800°C, but at magmatic temperatures and/or in samples with higher concentrations of H<sup>+</sup> in relatively unstable defects, the redistribution rates are likely to be higher. The coupling of rates, and potential for steady state, can be seen by coupling the reverse of equation 2 with equation 4:



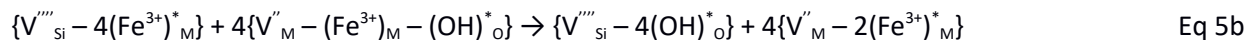
As H<sup>+</sup> loss proceeds at the redox rate from [Ti-2H], the number of anhydrous Si vacancies associated with [Ti-2Fe<sup>3+</sup>] increases, and so the redistribution of H<sup>+</sup> from [Si-4H] to [Ti-2H] becomes easier and thus faster. This increase in anhydrous Si vacancies is also likely to increase the rate of vacancy-facilitated diffusion of the H<sup>+</sup> in this [Si-4H] peak out of the crystal.

#### *Defect evolution during dehydration of Kilauea Iki olivine*

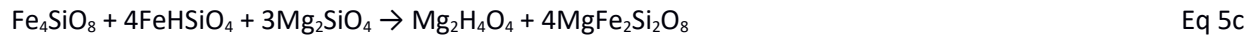
Figure 14 illustrates the potential initial defects and mode of H<sup>+</sup> reorganization in Kiki, and how different this is from San Carlos. After 8 hours of heating at 800°C, Kiki shows a clear decrease in the [tri-H] concentration and mirrored increase in [Si-4H], while the [Ti-2H] peaks and bulk H<sup>+</sup> were essentially immobile (Figure 9), in striking contrast to the clear loss in [Ti-2H] from San Carlos olivine SC1-2 under the same experimental conditions (Figure 7). These results suggest that Kiki underwent an initial redistribution of H<sup>+</sup> prior to H<sup>+</sup> loss (Figure 14A to 14B), described broadly as



which may be described in Kröger-Vink notation as



and in terms of olivine formula units as



After increasing the temperature to 1000°C, the [Ti-2H] exhibited fast, anisotropic loss profiles from Kiki (Figure 10). The reason for this jump in the [Ti-2H] movement rate, from essentially immobile (at or near the PV rate) to noticeable H<sup>+</sup> loss at the redox rate, is not entirely clear but may be related to the initial defect structure of Kiki. Unlike the San Carlos xenolith, the Kiki volcanic phenocryst was rapidly quenched in minutes in a fire fountain (Newcombe et al., 2017 IAVCEI abstract); moreover the magmatic host with which it equilibrated was significantly oxidized (FMQ+0.4, Helz et al., 2017). This would have led to an abundance of Fe<sup>3+</sup> in the initial Kiki, which might have impeded loss from Ti-defects (rev-Eqn 2) in the lower temperature experiments (800°C). At higher temperatures, the sphere of availability of Fe<sup>2+</sup> might have been greater, enabling H<sup>+</sup> to exit [Ti-2H] once again at the redox rate. equilibration in the redox state of the crystal.

### *Achieving steady-state rates between the redox rate and PV during dehydration*

We observe diffusivities significantly higher than those expected for vacancy-facilitated diffusion measured in synthetic forsterite (Figure 12), which suggests that at least one mechanism is occurring that involves only the movement of H<sup>+</sup> and electrons, the classic redox mechanism: 2H<sup>+</sup> + 2Fe<sup>2+</sup> → H<sub>2</sub> + 2Fe<sup>3+</sup> (Kohlstedt and Mackwell 1998). The relationship between this rapid process and purely vacancy-facilitated diffusion is traditionally understood in terms of the abrupt transition, a sort of light switch that is set to either on or off, at rates equal to either redox or PV. This clear transition has been observed for hydration (Kohlstedt & Mackwell 1998; Demouchy & Mackwell 2006; this study Figure 5), but our dehydration data are not fully consistent with this model in terms of either edge concentrations or the rate of change in the diffusivities. Thoraval and Demouchy (2014) model profiles expected for such a transition (their Figure 6). Their models predict a fairly close equivalent to the metastable equilibrium concentration of hydration, in which very early stage dehydration profiles are not particularly well developed near the edge, reach a stage in which the profile is relatively flat with very steep drops on the edges, and then proceeds to drop at the PV rate. The Kilauea Iki bulk H<sup>+</sup> profiles change very little during initial heating at 800°C, when Thoraval and Demouchy suggest that rapid redox rate diffusion should be occurring, and then at 1000°C we observe reasonably well developed profiles from earlier on that appear to go to zero and are fairly consistent over time. The SC1-2 data had an initial hydrated concentration at metastable equilibrium rather than full solubility and might be expected to only proceed at the redox rate until all of the H<sup>+</sup> had returned to its untreated level. Instead, the bulk H<sup>+</sup> diffusivity in SC1-2 appears to slow down over time. The behavior of H<sup>+</sup> thus appears to be fundamentally different during dehydration than what might be expected from hydration experiments. One possibility is that the initial rapid hydration of San Carlos at the redox rate is limited by the initial abundance of Fe<sup>3+</sup> in olivine, which is below detection limits for most techniques. Once the Fe<sup>3+</sup> is consumed, hydration at the redox rate (Eqn 2) must cease. This is not the case for dehydration, where wt% levels of Fe<sup>2+</sup> are always present to drive Eqn 2 backwards. Thus, while we see rate changes during dehydration that are likely due to the reorganization of H<sup>+</sup> and the effective proximity of Fe<sup>2+</sup>, there is no shut-down as in hydration.

We can also understand the difference in behavior for SC1-2 (decreasing diffusivities with time from fast to relatively slow) and Kiki at 1000°C (constant relatively slow diffusivities) as a difference in initial Fe<sup>3+</sup> concentrations, with SC1-2 starting with little active Fe<sup>3+</sup> (having just reduced the sample during hydration) and thus experiencing more initial H<sup>+</sup> loss at the redox rate. In contrast, redox-rate loss of H<sup>+</sup> may have been impeded in the significantly oxidized Kilauea Iki olivine (FMQ+0.4, Helz et al., 2017). Because of this decrease in the bulk H<sup>+</sup> diffusivity, the transition from the redox rate to the PV rate during dehydration is less like a light switch and more like a dimmer switch, with a top setting of the redox rate and bottom setting of PV.

However, this dimmer switch analogy is not perfect because, as described in the previous two sections, variations in H<sup>+</sup> diffusivities are also affected by changes in the ferric/ferrous ratio and a competition between dehydration and rehydration associated with H<sup>+</sup> redistributing among defect sites. The fact that we are able to come up with a common set of Arrhenius laws also suggests that at some point a steady state is reached intermediate between the redox rate and PV. We relate this steady-state rate to the coupling of Equations 2 and 4, in which the overall rate-determining step is the movement of H<sup>+</sup> from one site to another.

One alternative possible explanation for the apparent convergence of bulk H<sup>+</sup> rates is that the H<sup>+</sup> loss rate may be set by the rate at which the ferric/ferrous iron ratio equilibrates with the fO<sub>2</sub> external to the sample. Such re-equilibration is known to occur (Gaetani et al. 2012) and could reduce the Fe and allow redox-rate diffusion to continue where it might otherwise have stopped on account of a local over-abundance of Fe<sup>3+</sup>. Once the lattice of a given olivine's ability to accept Fe<sup>3+</sup> has been saturated, the redox-rate in that olivine will then be limited by the rate at which Fe<sup>3+</sup> can be re-introduced. However,

$fO_2$  equilibration in the center of the crystal may be slow (Faul et al., in revision), and  $H^+$  diffusivities have been consistently observed to be independent of  $fO_2$  (see Mackwell and Kohlstedt 1990, Kilauea Iki in this study, and the differences in  $fO_2$  among the melt inclusion studies shown in Figure 12) which suggest that the equilibration with the external  $fO_2$  during these experiments is too slow to have a significant impact on the measured diffusivities. However, the  $Fe^{3+}/Fe^{2+}$  ratio and total Fe content does appear to be important for determining  $H^+$  behavior (e.g., the difference between  $H^+$  movement in the Kilauea Iki and San Carlos olivines at 800°C). Thus, the initial  $fO_2$  at which a sample is initially equilibrated likely is important for determining the apparent  $H^+$  diffusivity, although the  $fO_2$  at which the experiment is conducted is not. The effect of total Fe concentration is more difficult to assess here because the forsterite numbers of our two samples are so similar (87.7 in San Carlos and 86.2 in Kilauea Iki).

#### *Comparison with previous work for bulk $H^+$*

Our final bulk  $H^+$  diffusivities for all three crystals (Figure 12) are consistent with the large majority of previous observations of  $H^+$  movement out of Fe-bearing olivines in nature. Thoraval and Demouchy 2014 extensively discuss 1- and 3-dimensional modeling of FTIR profiles of natural dehydrated olivine, with specific application to  $H^+$  profiles in Pali-aiki olivine measured by Demouchy et al. 2006 and including discussion of  $H^+$  profiles measured by Peslier and Luhr 2006 and Denis et al. 2013. They conclude “The concentration profiles measured for Pali-aiki samples are characteristic of dehydration. However, they are neither consistent with redox process, which is too fast, nor with PV process, since a fast [001] axis is not observed.” Profiles reported in Peslier et al. 2008 and Peslier et al. 2015 could also be reasonably interpreted as having a fast direction  $\parallel a$  rather than  $\parallel c$ . Our experimental results are fully consist with the many observations in natural samples of dehydration intermediate between redox and PV rates and with a fast direction  $\parallel a$ .

Our proposed Arrhenius laws are also consistent with the observation of  $H^+$  distribution in and around melt inclusions by Le Voyer et al. 2014 and Lloyd et al. 2013. Le Voyer et al. 2014 used the NanoSIMS to map bulk  $H^+$  around an olivine-hosted melt inclusion and found strongly anisotropic zonation with an inferred fast direction of H-loss parallel to  $a$ . They interpreted this observed anisotropy as dehydration at the redox rate, but the results presented here demonstrate that dehydration can occur with a fast direction  $\parallel a$  and diffusivities lower than redox. Lloyd et al. 2013 document water loss from olivine-hosted melt inclusions as a function of the size of the pyroclast. The decompression rates determined from melt embayments from the same samples (Lloyd et al., 2014) are more consistent with  $H^+$  loss from the melt inclusions through the olivine at close to the redox rate than to the PV rate and are consistent with our proposed Arrhenius laws.

Hauri 2002, Portnyagin et al. 2008, Chen et al. 2011, Gaetani et al. 2012, and Mironov et al. 2015 use changes in the water concentration in the melt inclusions in unoriented olivines to estimate  $H^+$  diffusivities in natural olivine. As discussed in some detail by Chen et al. 2011, diffusive anisotropy is very difficult to account for in these experiments, and the resulting estimates are likely to fall somewhere between the fast and slow direction diffusivities. Indeed, six of the seven diffusivity estimates produced from these melt inclusions studies fall between our estimated fast direction diffusivities  $\parallel a$  and our slower direction diffusivities (Figure 12). Thus, the  $H^+$  diffusivity estimates from Portnyagin et al. 2008, Chen et al. 2011, Gaetani et al. 2012, and Mironov et al. 2015 are all fully consistent with the results presented here. This agreement is remarkable given the wide variety of experimental conditions represented by these efforts, including both hydration and dehydration and oxygen fugacities ranging from QFM-7 (Chen et al. 2011) to QFM+3.3 (Portnyagin et al. 2008). Such similarity in inferred diffusivity over 10 log units of  $fO_2$  suggest either that  $fO_2$  does not affect  $H^+$  diffusivity (which we find unlikely, given the close coupling to Fe redox), or that externally imposed  $fO_2$  in many experimental assemblies does not equilibrate with the sample interior as rapidly as  $H^+$  reacts and moves through the lattice. The latter view is supported by recent work of Faul et al. (in revision) that suggests  $fO_2$  equilibration may proceed

at the slower rate of metal vacancy diffusion, and thus will be incomplete in many laboratory experiments.

The only exception to the broad agreement of the above studies is a single, very fast estimate by Hauri 2002 for the dehydration of a melt-inclusion-bearing olivine from Loihi. This very rapid movement is difficult to understand with any certainty in the absence of either oriented profiles or FTIR spectra, and in the absence of measurements of crystal or melt inclusion sizes. The diffusivities calculated in Hauri 2002 also did not take into account the very low partitioning of water in olivine, which plays an important role in impeding melt inclusion water loss through the olivine (e.g., Chen et al., 2011). We conclude that the diffusivity determined in Hauri 2002 is highly uncertain and could reflect rates similar to those inferred for the other studies of melt inclusion re-equilibration shown in Figure 12.

Finally, we also note a coherence between our proposed Arrhenius laws and those for H-D self-diffusion, determined by DuFrane and Tyburczy (2012) and Novella et al. (2017). In these experiments, San Carlos was first dry-annealed, then wet annealed at the redox rate, then wet annealed again within a bath of heavy H<sub>2</sub>O. The rate at which D entered the olivine was interpreted as the H-D exchange rate, and proceeded along Arrhenius laws remarkably similar to ours for dehydration (Figure 12). Given that the mechanism of H loss and D gain is largely one of exchange between defect sites, this may be similar to the rate of reorganization that we have interpreted to be the control on bulk H loss from olivine.

While more work remains to better understand and predict the variations in the rate of H loss from olivine, the frequent observation of rapid H<sup>+</sup> loss and anisotropy from natural samples suggests that at least some of the H<sup>+</sup> in a typical olivine dehydrating upon ascent is exiting at the redox rate, resulting in H<sup>+</sup> diffusion with a fast direction ||  $a$ . In almost all cases, the bulk diffusivity of H<sup>+</sup> in olivine occurs at rates between the redox and the PV rates.

#### *Comparison with previous work on peak-specific behavior*

H<sup>+</sup> loss or gain occurs from different FTIR peaks at different rates (Figures 7-10; Padron-Navarta et al. 2014; Hilchie et al. 2014; Tolland et al. 2015; Peslier et al. 2015; Jollands et al. 2016). Most of the peak-specific H<sup>+</sup> diffusivities observed in this study are orders of magnitude higher than any of the diffusivities observed in synthetic forsterite (Figure 12). Peak-specific diffusivities may also change over time (Figure 8), most likely due to a redistribution of H<sup>+</sup> among different defects and discussed further below. Thus, single values for peak-specific diffusivities measured in synthetic forsterite (Padron-Navarta et al. 2014; Jollands et al. 2016) are unlikely to apply to natural Fe-bearing olivines where H<sup>+</sup> movement at or near the redox rate is taking place, and an increased number of defects and higher vacancy concentrations may speed up vacancy-facilitated diffusion.

Padron-Navarta et al. 2014, Hilchie et al. 2014, and Peslier et al. 2015 all observe faster movement of Mg-vacancy-related defects [Mg-2H] and/or [tri-H] relative to Si-vacancy-related defects [Ti-2H] and [Si-4H] during dehydration. This observation is echoed in our hydration data for SC1-7 (Figure 5) but we were unable to test this result during dehydration of our SC1-2 sample because these peaks were either not present ([Mg-2H]) or not systematically present ([tri-H]).

During the sequential dehydration of the Kilauea Iki olivine, we observe a clear fast direction ||  $a$  in [Si-4H] and [Ti-2H] but not the [tri-H] peaks, which produce noisy, isotropic profiles with diffusivities that are, while still faster than would be expected from vacancy-controlled diffusivities in forsterite, roughly an order of magnitude slower ||  $a$  than the [Ti-2H] and [Si-4H] peaks, in contrast to the observations of faster [tri-H] movement by other authors. The difference in anisotropy also suggests that the dominant mechanism by which H in our Iki sample leaves [tri-H] is different from how it leaves [Ti-2H] and [Si-4H]. Perhaps, for instance, H leaves [Ti-2H] and [Si-4H] primarily at the redox rate but leaves [tri-H] primarily during some redistribution process, for instance by moving from a Mg vacancy to a Si vacancy.

The SC1-2 partial hydration to metastable equilibrium resulted in minuscule amounts of [Mg-2H] and [tri-H] (Figures 4 and 5) too small to give meaningful diffusivities during dehydration. The absence of

these peaks from SC1-2 and large increase in [Ti-2H] suggest that in San Carlos olivine, the vast majority of H<sup>+</sup> diffusion at the redox rate is affecting the [Ti-2H] specifically. This observation is in stark contrast to > 4 orders of magnitude lower rate of [Ti-2H] dehydration measured by Padron-Navarta et al. (2014) in Fe-free synthetic forsterite. This result underscores the lack of inherent peak-specific rates, and the importance of Fe in allowing H to exit quickly from any site via reorganization (similar to our results for clinopyroxene, Ferriss et al., 2016). Padron-Navarta et al. (2014) found a similar importance for reorganization, where [Si-4H] initially dehydrated as rapidly as [Ti-2H]. But without Fe, all diffusivities were limited to the next fastest rate, that of metal vacancies. The fact that H<sup>+</sup> is able to enter San Carlos olivine so quickly in the first hours of hydration at the redox rate suggests that at least some octahedral Ti is initially present in San Carlos olivine. If all of the Ti were on the tetrahedral site initially, then some of that Ti would need to change its position in the crystal to create the [Ti-2H] defect, a process that is unlikely to occur under the hour timescales at which diffusion is observed. The presence of octahedral Ti in San Carlos olivine may be explained by slow hydration reactions that require octahedral Ti occurring at depth (e.g., following the reverse of the reaction described by Padron-Navarta et al. 2014 Eq 3b) followed by rapid dehydration and quenching in a lava flow. Thus, any rapid influx of H<sup>+</sup> at the redox rate into an olivine may be limited not only by the initial quantity of Fe<sup>3+</sup> (Kohlstedt and Mackwell 1998) but the initial amount of octahedral Ti.

The convergence of peak-specific rates in San Carlos olivine (Figure 8) suggests that in some applications peak-specific behavior may be safely ignored. An important exception may be the high-wavenumber [Si-4H] peaks such as 3600 cm<sup>-1</sup> peak in the San Carlos olivine described here and the 3613 cm<sup>-1</sup> peak in forsterite described by Padron-Navarta et al. 2014. These peaks never came close to a rim concentration of zero in either of these experiments, and was particularly slow moving during early stages of dehydration. However, the 3600 cm<sup>-1</sup> peak first rises (at 800°C) and then drops (at 1000°C) significantly in the Kilauea Iki olivine, indicating that it can sometimes increase or decrease relatively rapidly. Additional work to understand peak-specific behavior is warranted, and any workers concerned with H<sup>+</sup> diffusion in or out of olivine or olivine-hosted melt inclusions should routinely obtain polarized FTIR profiles to help determine the importance of differences in individual peak behavior for a given olivine.

## Conclusions

We conducted a series of hydration and dehydration experiments to gain insight into the behavior of H<sup>+</sup> in natural olivine. The results show strikingly different behavior from previous studies, which focused on either hydration only, or on Fe-free olivine. We also discovered a rich range of behavior even for just the two olivines used in our study. H<sup>+</sup> can speed up or slow down as it exits olivine, and move at rates that depend on the evolving defect structure. Nonetheless, our results point to a common working rate of H loss for most natural olivines that will be useful in a range of applications. While there is still much that we do not understand, and more work is welcomed on the experimental dehydration of a range of olivine compositions and on the analytical challenge of measuring Fe<sup>3+</sup> in olivine, we can however draw three conclusions with some certainty.

First, there is no inherent diffusivity for specific H defects in olivine. For example, the important Ti-clinohumite defect in olivine, [Ti-2H], which may host much of the water in mantle olivines, loses H<sup>+</sup> at a rate that can vary by more than 4 orders of magnitude, depending upon the Fe concentration and local Fe<sup>2+</sup>/Fe<sup>3+</sup> distribution. We found that [Ti-2H] can dehydrate or hydrate at or near the fastest redox rate in olivine. H<sup>+</sup> movement into and out of this defect at these very fast rates requires that the Ti be present initially in an octahedral rather than tetrahedral site because the movement of H<sup>+</sup> is too rapid to allow for a reaction to occur in which Ti, or any other large ion, can move between sites. Thus, rapid hydration of olivine depends at least partially on the initial concentration of octahedral Ti. In the case of

San Carlos olivine, which is commonly studied, its cooling history may already have pre-conditioned it for rapid hydration, due to rapid cooling and dehydration in lava that froze in octahedral Ti already associated with Fe<sup>3+</sup>.

Second, the rates at which both bulk H<sup>+</sup> and individual defects sites move can change over time and depending on the defect structure of the crystal. Thus, the use of constant peak-specific diffusivities measured in synthetic forsterite, e.g., as measured by Padron-Navarta et al. 2014 and applied in Tollar et al. 2015, is inappropriate for natural, Fe-bearing samples. Further, the changes in bulk H<sup>+</sup> diffusivities observed here for dehydration are different from those observed here and elsewhere for hydration. Moreover, the binary change of rates from redox to proton-vacancy suggested by Thoraval & Demouchy 2014 based on observations of hydration are not observed in our dehydration experiments. Instead, the buildup of Fe<sup>3+</sup> and redistribution of H<sup>+</sup> defects effectively slow down dehydration from redox rates.

Third, there appears to be a common set of Arrhenius laws that can be used to explain most experimental and natural data for H<sup>+</sup> loss from Fo~90 olivine:  $D_{[100]} = 10^{-5.4} \cdot \exp(130/RT)$ ;  $D_{[010]} = 10^{-6.9} \cdot \exp(130/RT)$ ; and  $D_{[001]} = 10^{-6.6} \cdot \exp(130/RT)$ , where the units of the diffusivities are in m<sup>2</sup>/s, and the activation energy, 130, is in kJ/mol. These Arrhenius laws are intermediate between the classic redox and PV models of diffusivity observed during hydration and are in good agreement with many observations of a fast direction ||  $\alpha$  in natural olivine. While variations in different H<sup>+</sup> incorporation mechanisms and other defects may produce potentially large variations in the bulk H<sup>+</sup> diffusivities for different olivines, the working bulk H<sup>+</sup> Arrhenius laws determined here are expected to apply to most natural olivines.

Our results on H<sup>+</sup> diffusion in olivine find close parallels in the study of pyroxenes. Woods et al. (2000) point to an important threshold Fe content that leads to rapid bulk H diffusion in clinopyroxene. Stalder and Skogby (2007) demonstrate the importance of rapid reaction between defects, reorganization and redox reactions, documented by Mossbauer spectroscopy, during hydration and dehydration of Fe-bearing enstatite. Our own work (Ferriss et al., 2016) shows how peak-specific diffusivities become less important, and uniformly faster and approach the redox rate, with greater Fe content in clinopyroxene.

There is good news and bad news in the uniformly rapid rates of H<sup>+</sup> loss from olivine during ascent and cooling. The bad news is that olivine in mantle xenoliths are likely to equilibrate on time scales of minutes to hours rather than days, as suggested by previous work on dehydration of synthetic forsterite (Padron-Navarta et al. 2014). Thus, it is possible that the H<sup>+</sup> in olivine from many xenoliths has re-equilibrated with the host magma during the hours to days of transport to the surface (Ferriss et al., 2016). Systematic study of mantle xenoliths and host magmas are necessary to assess this possibility. The good news, however is that H<sup>+</sup> profiles in olivine, both phenocrysts and in xenoliths, are of great practical use for ascent chronometry. With the H<sup>+</sup> diffusivities known, measurements of H<sup>+</sup> profiles in olivine can now be used to access hours-to-minute timescales of magma ascent prior to explosive eruptions (Newcombe et al., 2017).

## Acknowledgments

This work was supported by National Science Foundation grant #1449699. David Kohlstedt and David Ferguson provided the samples. Daniel Rasmussen performed the electron microprobe analyses. Maura Weathers, Henry Towbin, and Anna Barth performed the Laue Camera and EBSD analyses to confirm sample orientations. Erik Hauri performed the nanoSIMS analyses as part of a Cooperative

Institute for Dynamic Earth Research (CIDER) working group on the electrical conductivity of hydrous olivine.

## Figures

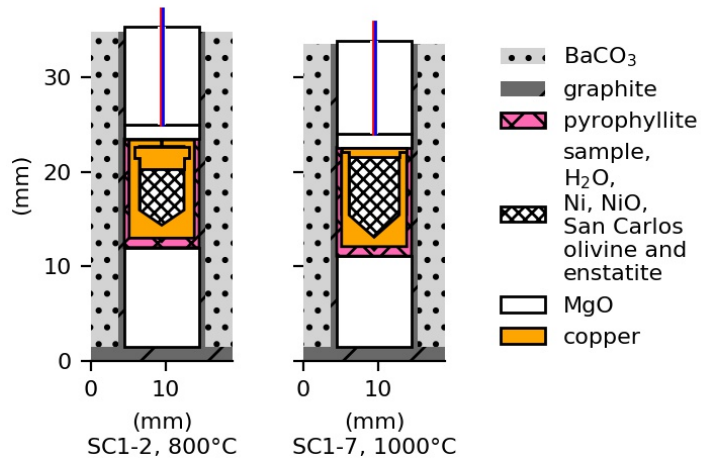


**Figure 1.** Schematic cross-sections illustrating the experimental design for hydrating San Carlos olivine samples SC1-2 and SC1-7 in a piston cylinder apparatus showing the BaCO<sub>3</sub> pressure medium, graphite furnace and pyrophyllite sleeve surrounding an unwelded copper capsule containing the sample, liquid water, and a powdered mixture of nickel, nickel oxide, San Carlos olivine, and San Carlos enstatite. The sleeve and capsule are supported by MgO, and D-type W-Re thermocouples (colored lines) extend through cylindrical holes in the MgO. Minor differences in the capsule shapes are a result of differences in Cu machining techniques.

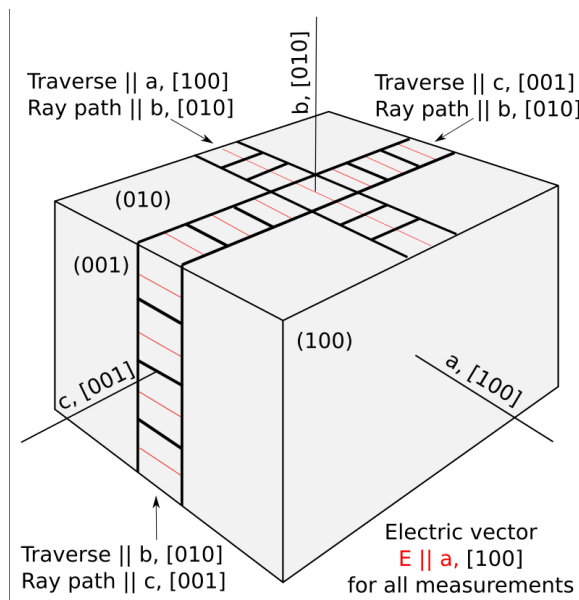


**Figure 2.** Schematic illustration of the orientations of the traverses, ray paths, and electric vectors used to collect FTIR profiles for diffusion modeling, including standard Miler indices and labels *a*, *b*, and *c* used throughout the text and figures.

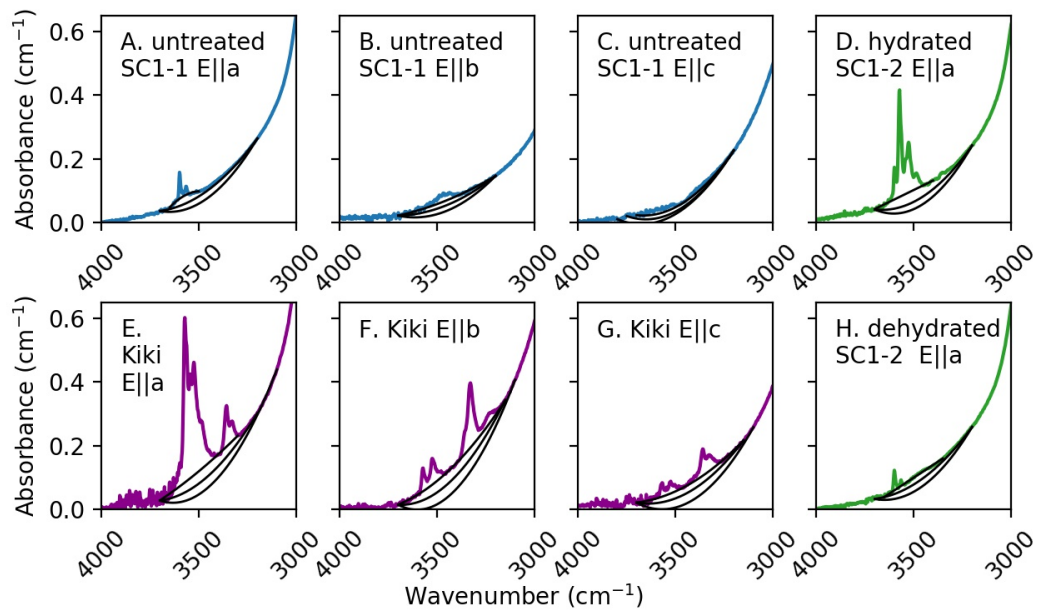


Figure 3. Polarized FTIR spectra and baselines (black) used to estimate the  $\text{H}^+$  concentrations of Kilauea Iki olivine (Kiki) and San Carlos olivine (SC1-1 and SC1-2) reported in Table 2. E is the electric vector of the infrared beam. Expanded views with peaks labeled are available in Figs 4 and 6 and the Supplement.

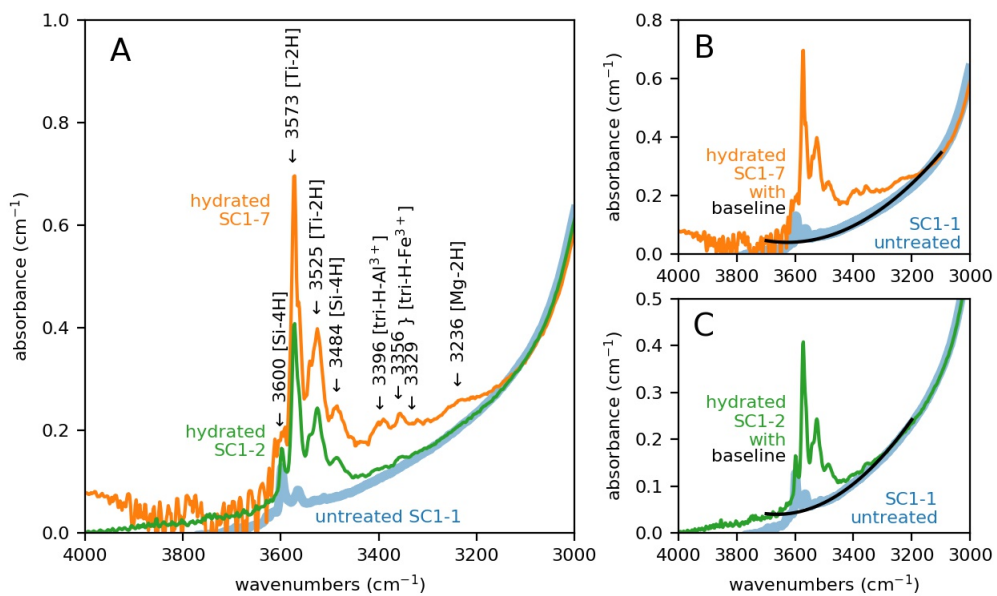
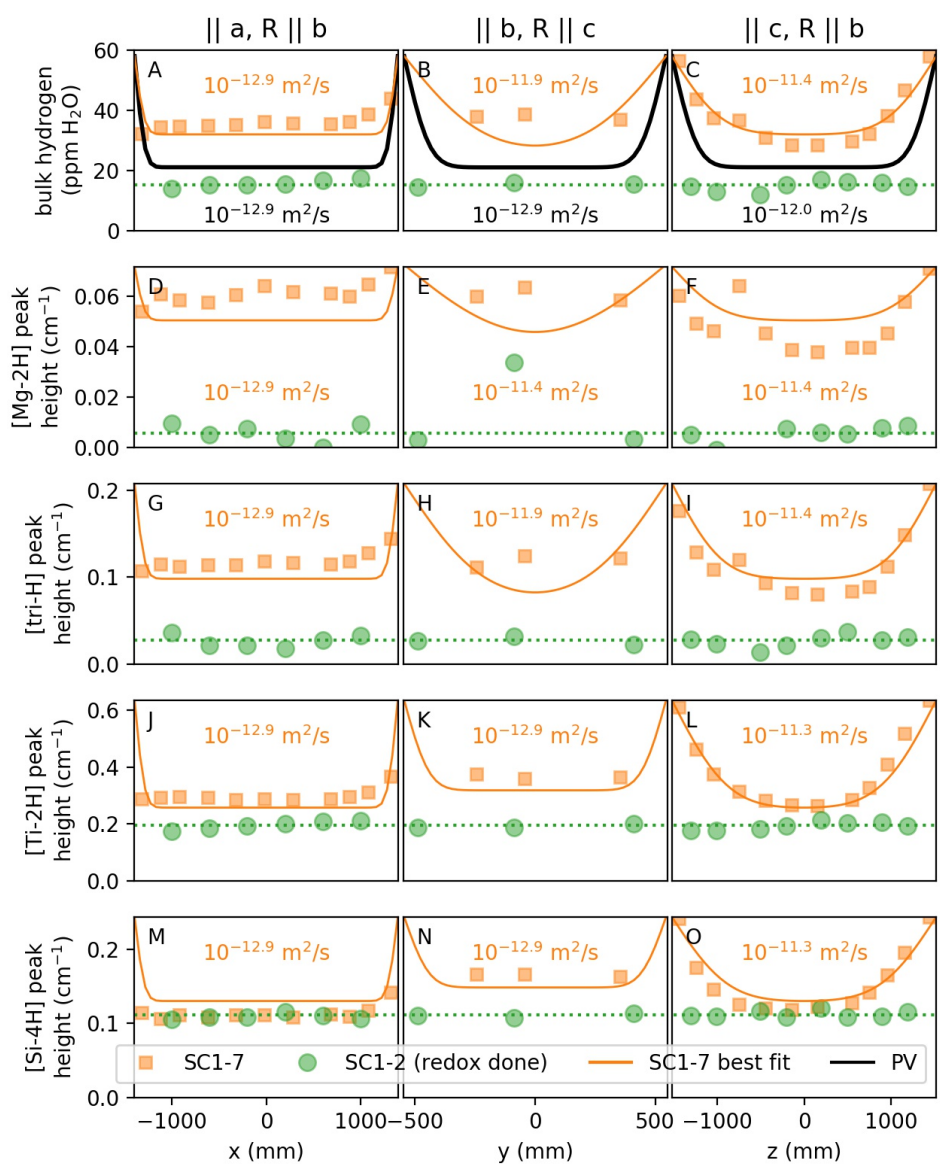


Figure 4. (A) Polarized FTIR spectra with electric vector  $E \parallel a$  averaged across all traverses in three directions of San Carlos olivine SC1 pieces that were untreated (SC1-1, blue); hydrated in a piston cylinder for exactly the amount of time needed to reach metastable equilibrium at the redox rate (SC1-

2, green) at 800°C; and hydrated long enough to enter into PV-rate diffusion without saturating the sample (SC1-7, orange) with major peaks labeled. The shapes of the quadratic baselines used to calculate the areas under each curve for spectra measured are shown for SC1-7 (B) and SC1-2 (C). Note the differences in the y-axis scale.



**Figure 5.** Concentration profiles across San Carlos olivine samples SC1-2 and SC1-7 after partial hydration in a piston cylinder as measured through the uncut block. R is the ray path of the infrared beam, and the electric vector E of the polarized beam is in all cases  $\parallel a$ .  $H^+$  concentrations are estimated from polarized FTIR spectra using the areas under the baselines shown in Figure 3 and initial  $H^+$  contents from Table 2. Black numbers and curves show the expected diffusion curves based on the diffusivities (D) for proton-vacancy (PV) rate diffusion at 1000°C, an initial metastable equilibrium concentration equal

to the mean concentration or peak height in the hydrated SC1-2 (dotted green lines, where all diffusion possible by the proton-polaron (redox) mechanism has been completed) and final concentration of 58 ppm  $H_2O$ . Thin orange lines show curves for the reported diffusivities, assuming the same initial and final concentration as the PV lines. The large difference between the black and orange curves in panel A despite their having the same diffusivity is a result of path integration effects along the ray path, *b*, which has significantly different diffusivities for the two models. See Ferriss et al. 2015 for a more complete discussion of this “whole-block” effect.

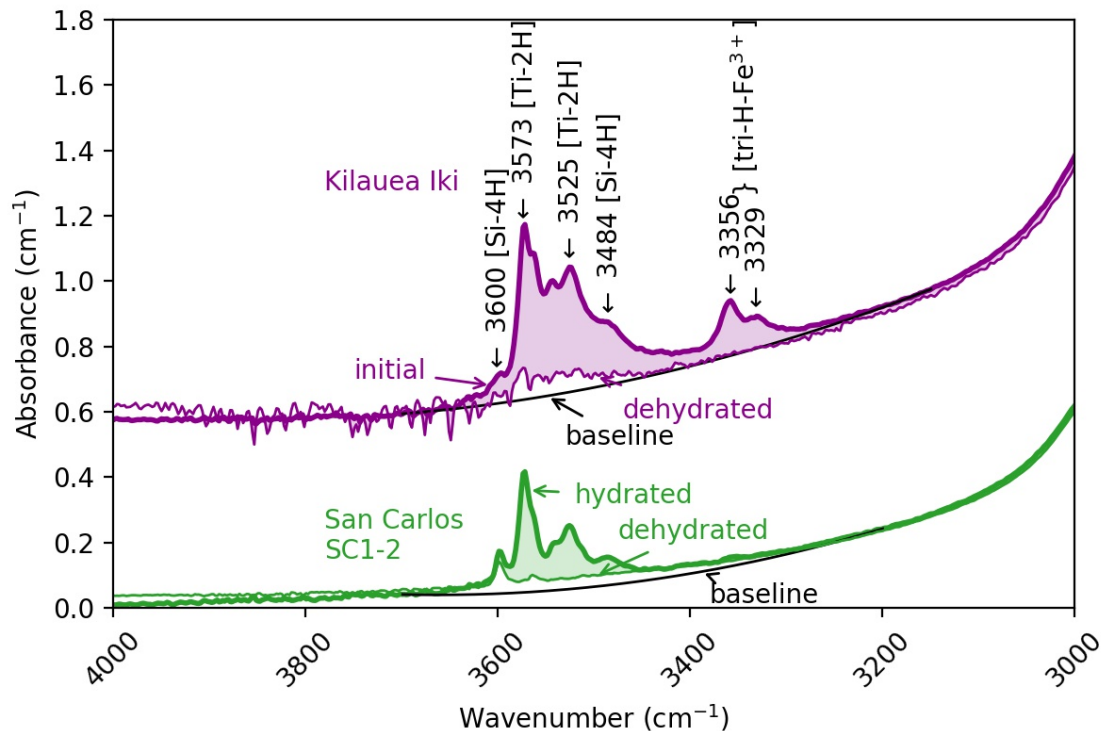
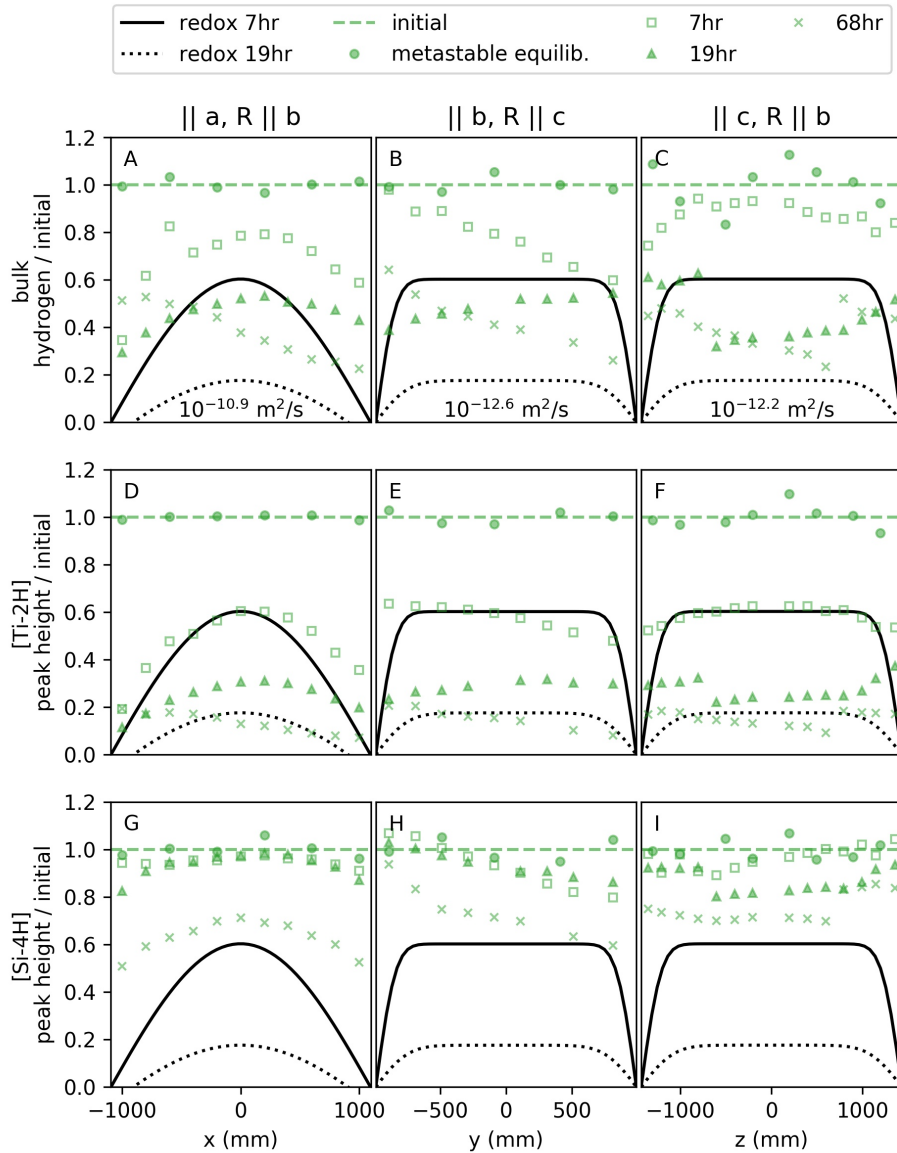


Figure 6. Averaged polarized FTIR spectra with electric vector  $E \parallel a$  of Kilauea Iki olivine (offset for clarity) and partially hydrated San Carlos olivine SC1-2 before and after heating in a gas-mixing furnace.



**Figure 7.** Path-integrated profiles of (A-C) bulk H, (D-F) the [Ti-2H] peak at 3525  $\text{cm}^{-1}$ , and (G-I) the [Si-4H] peak at 3600  $\text{cm}^{-1}$  during step-wise dehydration of an uncut block of partially hydrated San Carlos olivine SC1-2 at 1 atm, 800°C, and NNO-2.6. R is the ray path of the infrared beam. All data are normalized to a best-fit line through the hydrated profile data to account for small amounts of initial zonation. Black lines show expected hydrogen loss curves at the proton-polaron rate (diffusivities labeled in A-C). The redox rate is somewhat too fast to describe the bulk H data and much too fast to describe the [Si-4H] peak data. The [Ti-2H] data is very well described by the redox rate after 7 hours of

heating, but [Ti-2H] movement slows down by 19 hours. Baselines and best-fit diffusivities and curves are provided in the Supplemental PDF.

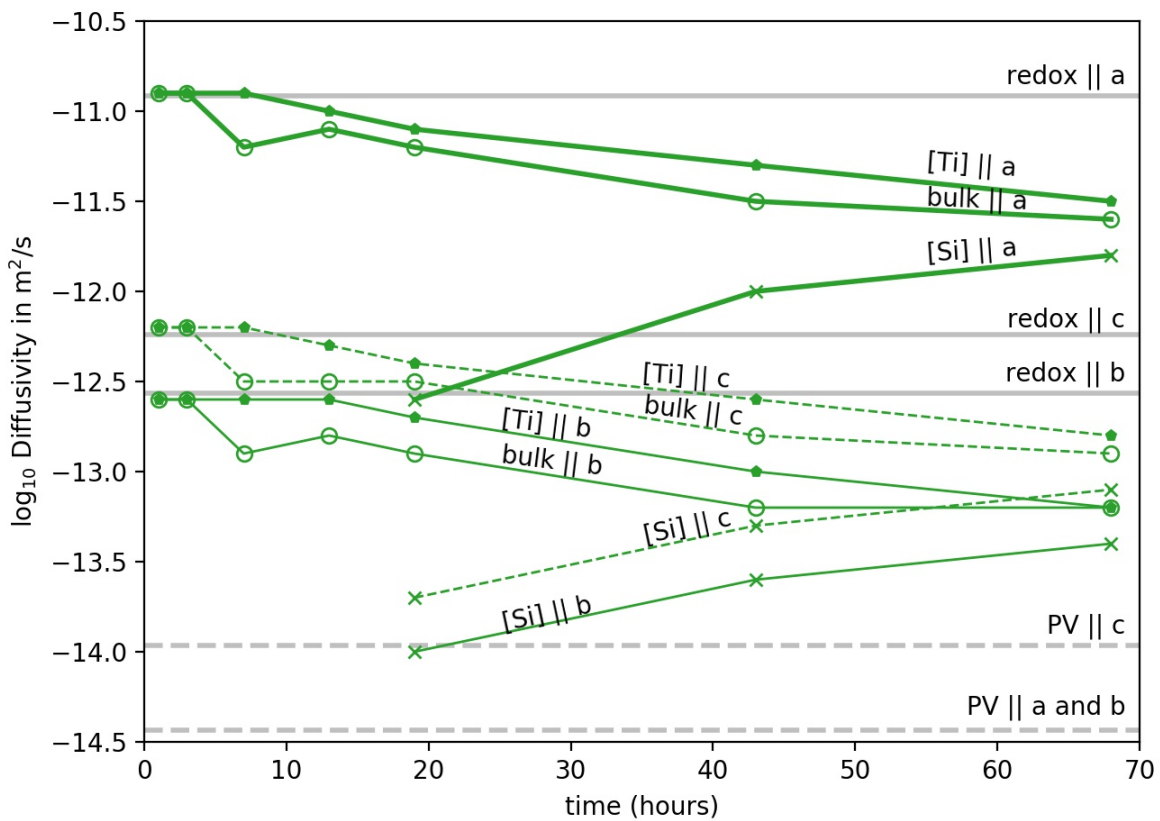


Figure 8. Estimated rates of  $\text{H}^+$  movement represented as diffusivities in San Carlos olivine SC1-2 with heating time at 800°C and oxygen fugacity of  $10^{-16.5}$  bars (NNO-2.6) in three crystallographic directions for bulk  $\text{H}^+$  and two peak-specific mechanisms described in the text,  $[\text{Si}-4\text{H}]$  and  $[\text{Ti}-2\text{H}]$ , compared with expected diffusivities for the proton-polaron, or redox, rate. Errors on all diffusivities (provided in Supplement) are omitted for clarity. The anisotropy of the observed diffusivities and redox is similar, with movement  $\parallel a > c > b$ , but the exact values are not consistent over time. At early heating stages, the bulk  $\text{H}^+$ , which is dominated by the mechanism  $[\text{Ti}-2\text{H}]$ , is consistent with expected redox values, but over time those diffusivities decrease. In contrast, the  $[\text{Si}-4\text{H}]$  mechanism is initially too slow to be measured confidently, but after 19 hours enough movement could be observed for fitting. These  $[\text{Si}-4\text{H}]$  diffusivities increased at 43 and 68 hours, approaching the values for  $[\text{Ti}-2\text{H}]$  and bulk  $\text{H}$ . The profile data used to obtain these diffusivities are shown in Figure 7 and the Supplement.

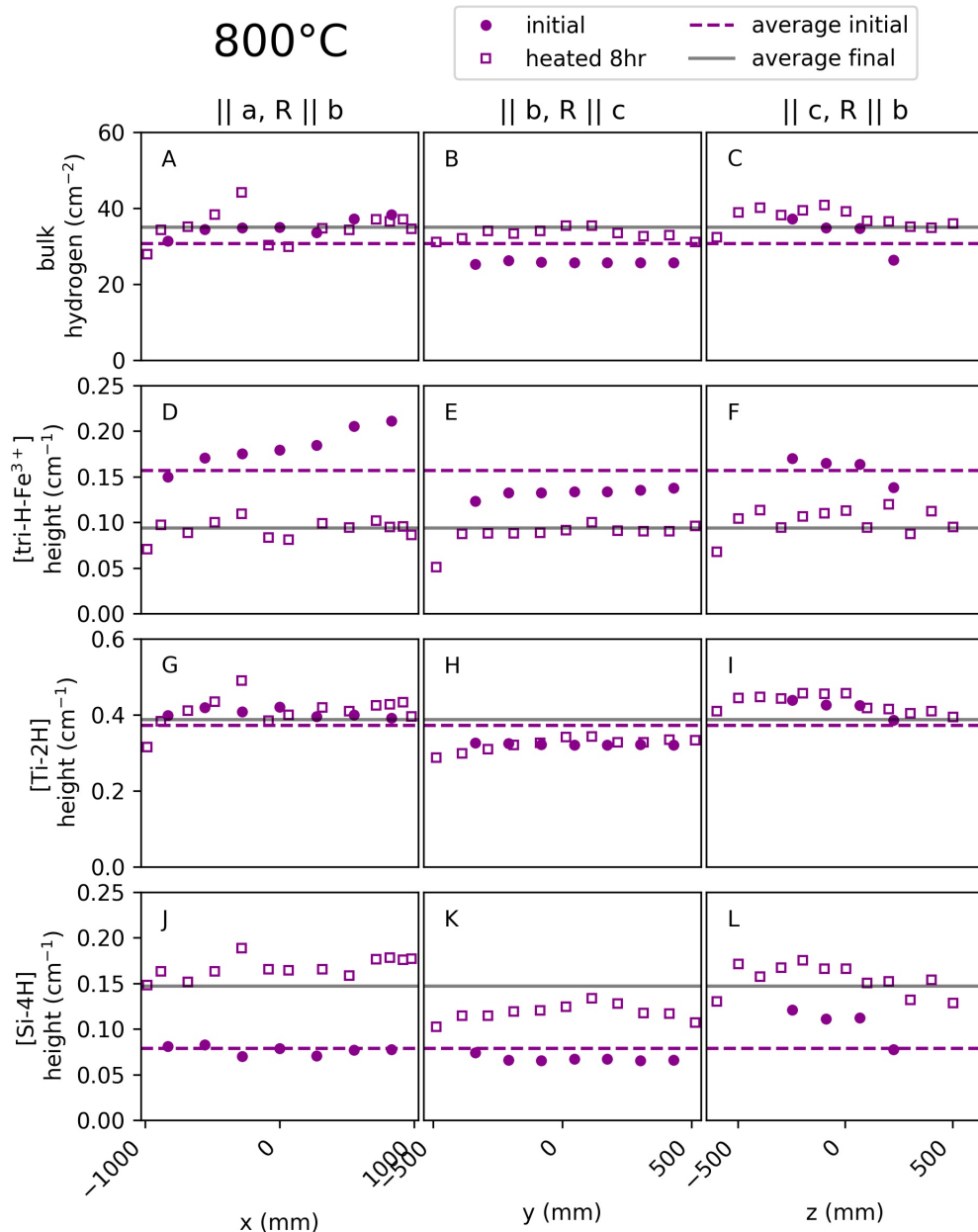


Figure 9. Path-integrated profiles of (A-C) bulk  $\text{H}^+$ , (D-F) the [tri-H] peak at  $3356 \text{ cm}^{-1}$ , (G-I) the [Ti-2H] peak at  $3525 \text{ cm}^{-1}$ , and (J-L) the [Si-4H] peak at  $3600 \text{ cm}^{-1}$  in an uncut block of Kilauea Iki olivine after 8 hours of heating at 1 atm and  $800^\circ\text{C}$ . R is the ray path of the infrared beam. The increase in the average [Si-4H] peak height of  $0.06 \text{ cm}^{-1}$  is similar to the decrease in the average peak height of the [tri-H] peak. The apparent increase of 4 ppm  $\text{H}_2\text{O}$  in the bulk  $\text{H}^+$  is small enough (15% change) to be within error of the initial.

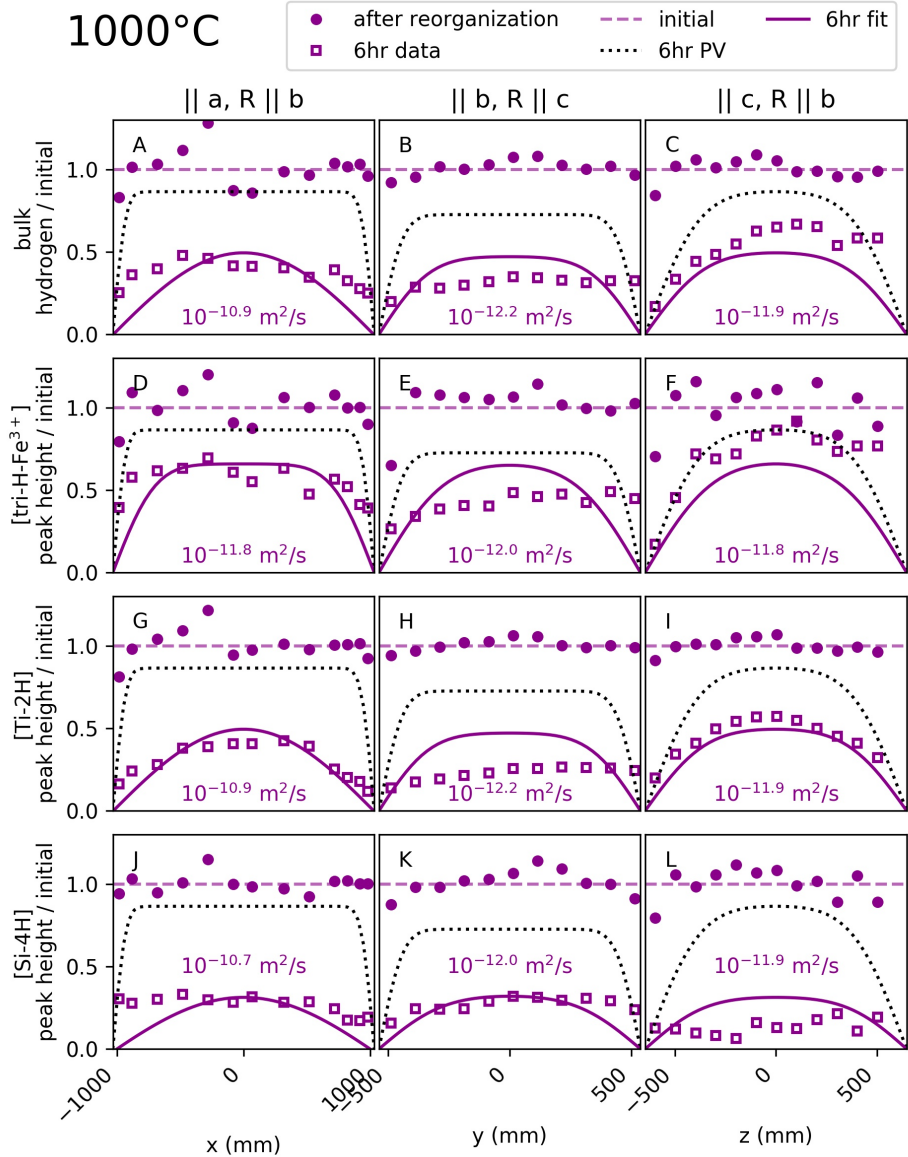


Figure 10. Path-integrated profiles of (A-C) bulk  $\text{H}^+$ , (D-F) the  $[\text{tri}-\text{H}]$  peak at  $3356 \text{ cm}^{-1}$ , (G-I) the  $[\text{Ti}-2\text{H}]$  peak at  $3525 \text{ cm}^{-1}$ , and (J-L) the  $[\text{Si}-4\text{H}]$  peak at  $3600 \text{ cm}^{-1}$  in an uncut block of Kilauea Iki olivine after 6 hours of heating at 1 atm and  $1000^\circ\text{C}$ . R is the ray path of the infrared beam. All profiles are normalized to profile data measured after heating for 8 hours at 1 atm,  $800^\circ\text{C}$ , and NNO-2.6, which produced significant re-organization of the hydrogen across different sites (Figure 8). Numbers are the diffusivities that correspond to the purple lines fit to the data. The proton-vacancy rate (PV, dotted lines) is too slow to account for all of the observed  $\text{H}^+$  movement. If  $\text{H}^+$  were decreasing at the proton-polaron rate, redox, then all  $\text{H}^+$  would have been lost from the crystal. Baselines and best-fit diffusivities and curves are provided in the Supplement. Note the differences in x-axis scales and that this data is measured through the uncut block, and therefore measurements in the center of each profile may differ along different ray paths.

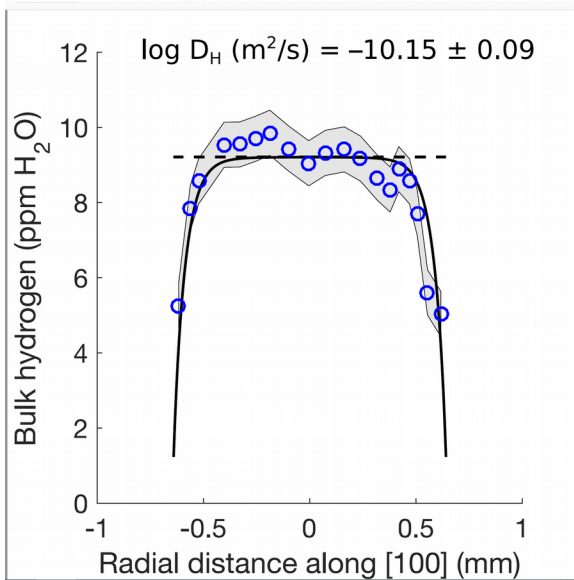


Figure 11.SIMS measurements of bulk H<sup>+</sup> along  $a$  in a Kilauea Iki olivine phenocryst and best-fit diffusivity at 1200°C based on Monte Carlo modeling and a 1D diffusion model. The grey envelope shows the data plus/minus 2 standard deviations, which is 0.6 ppm H<sub>2</sub>O.

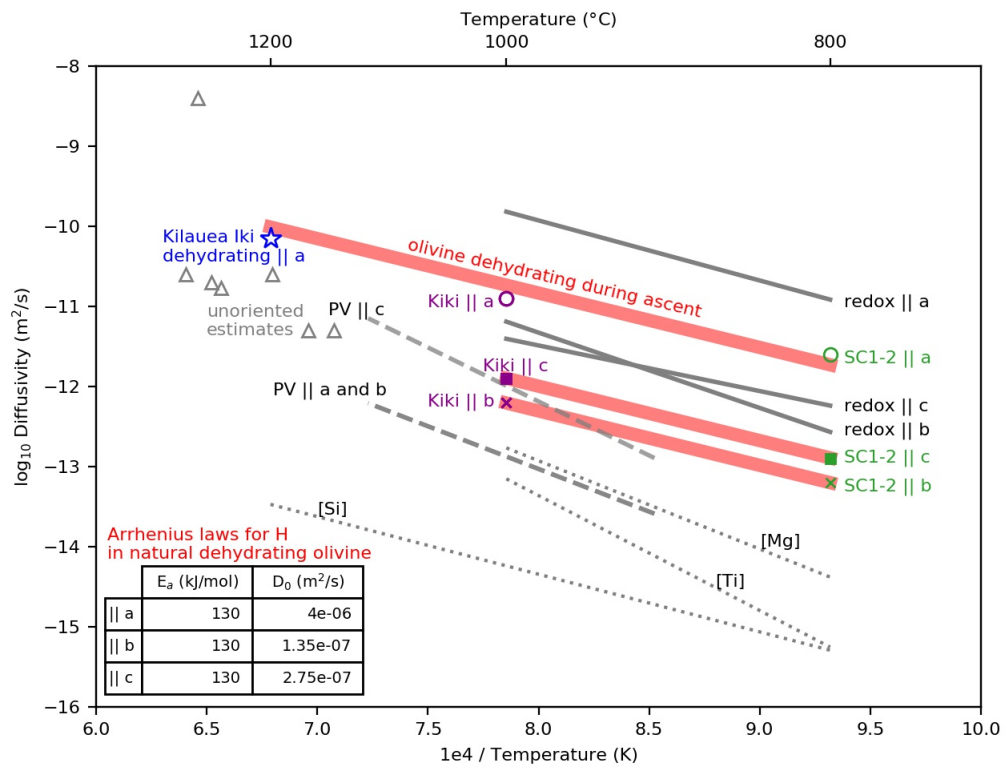


Figure 12. Arrhenius diagram for bulk H movement in olivine. Black lines show ranges for previous measurements of the proton-polaron rate (redox) and the proton-vacancy rate (PV) during hydration of San Carlos olivine as well as peak-specific measurements from the dehydration of synthetic forsterite (dotted lines, Padrón-Navarta et al. 2014). Pink line shows a fit through the final observed bulk H diffusivity measurements from this study: the experimental dehydration of San Carlos olivine at 800°C (SC1-2, green), the experimental dehydration of Kilauea Iki olivine at 1000°C (Kiki, purple), and the estimated diffusivity in Kilauea Iki || [100] during its ascent at 1200°C (blue star). Six out of seven independent estimates for bulk H diffusivity in unoriented melt-inclusion-bearing olivines (gray triangles; 1 data point from Portnyagin et al. 2008 and Mironov et al. 2015; 4 data points from Chen et al. 2011; and 1 data point from Gaetani et al. 2012) fall between and so our consistent with these fits. The exception is a higher diffusivity estimate by Hauri 2002 for an olivine from Loihi. The activation energies ( $E_a$ ) and pre-exponential factors ( $D_0$ ) for our fits are provided in the inset table. An interactive Arrhenius diagram that includes additional measurements and all time-series and peak-specific data is available online at <https://arrheniusdiagram.herokuapp.com>.

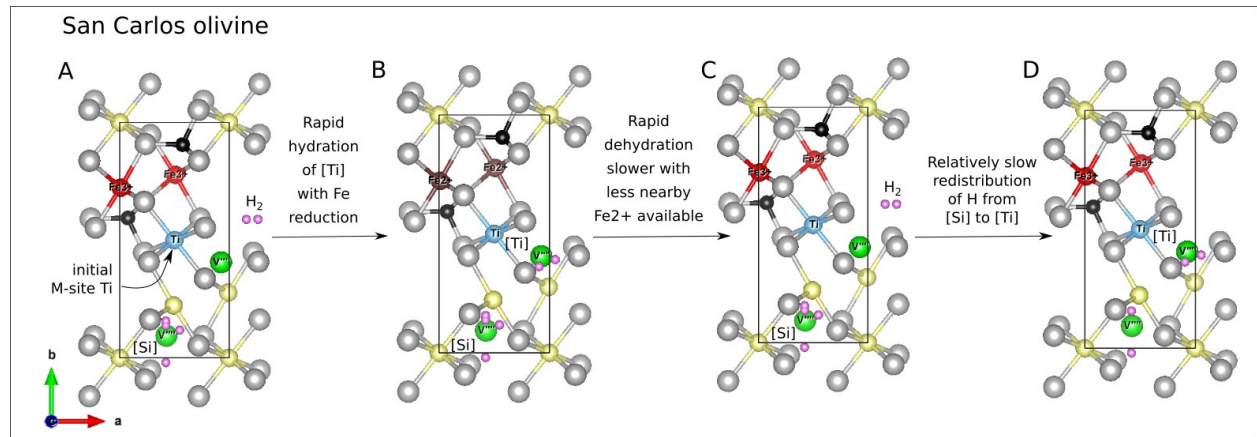


Figure 13. Crystal models of olivine viewed down the *c* axis to illustrate defects in San Carlos olivine (A) prior to treatment, (B) after hydration in a piston cylinder, (C) after the rapid initial stages of dehydration in a gas-mixing furnace, and (D) after continued heating resulting in partial redistribution of H<sup>+</sup>. Ball colors corresponds to the following: yellow is Mg; grey is O; black is Si; bright green is a Si vacancy; blue is Ti, pink is H, red is Fe<sup>3+</sup>, and brown is Fe<sup>2+</sup>. H positions and the substitution of Ti on an M1 site were selected following Walker et al. 2007 but are intended to provide a simple illustration of the reactions described in Eq 2 and 4, not to show definitive locations for all atoms in the structure.

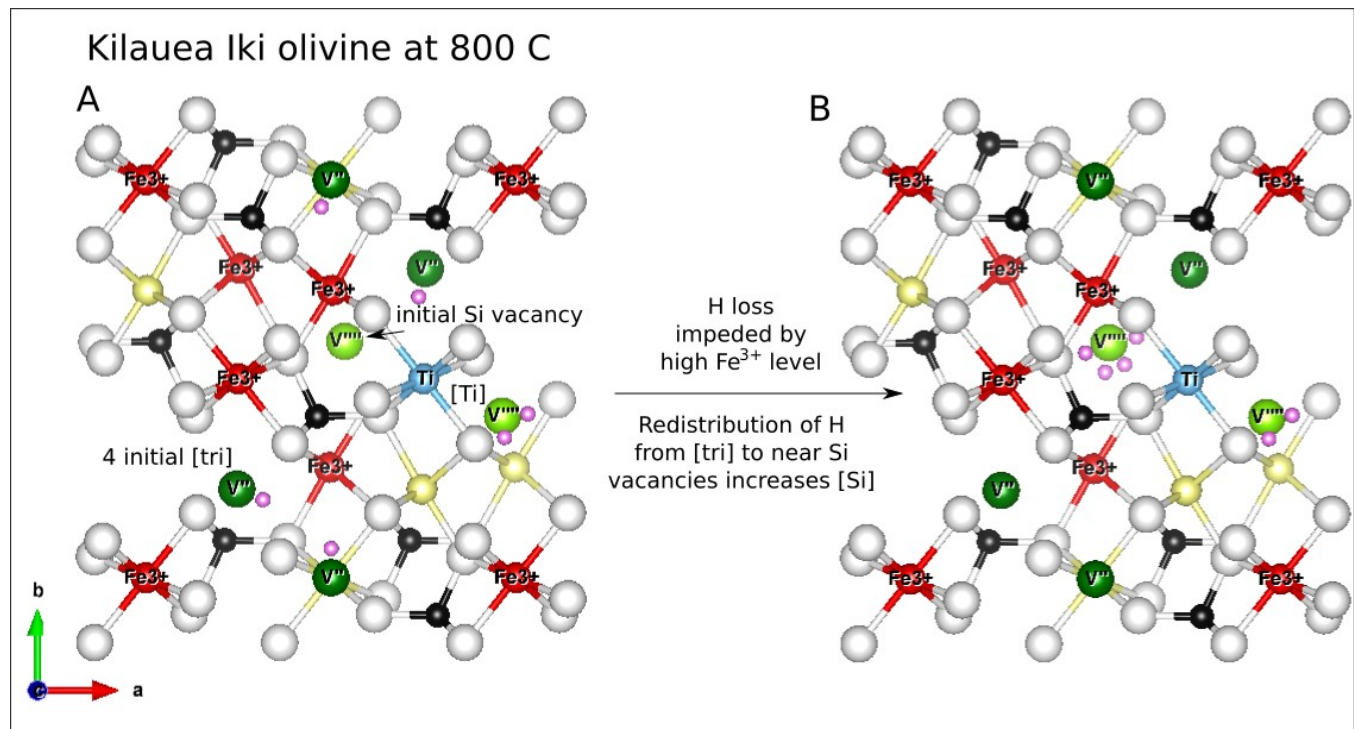


Figure 14. Crystal models illustrating defects in the Kilauea Iki olivine before (A) and after (B) heating at 800°C for 7 hours in a 1-atm gas-mixing furnace. Ball colors corresponds to the following: yellow is Mg; grey is O; black is Si; bright green is a Si vacancy; dark green is a metal site vacancy; blue is Ti, pink is H, red is Fe<sup>3+</sup>, and brown is Fe<sup>2+</sup>. Note that this figure is intended only to provide a general illustration of the defects and reaction described in Eq 5, and Fe<sup>3+</sup> is likely to be much less concentrated in a real crystal.

## Bibliography

- Bell, D. R., and G. R. Rossman  
1992 Water in Earth's Mantle: The Role of Nominally Anhydrous Minerals. *Science* 255(5050). WOS:A1992HH74400043: 1391–1397.
- Bell, D. R., G. R. Rossman, J. Maldener, D. Endisch, and F. Rauch  
2003 Hydroxide in Olivine: A Quantitative Determination of the Absolute Amount and Calibration of the IR Spectrum. *Journal of Geophysical Research-Solid Earth* 108(B2). WOS:000181985400002. ://WOS:000181985400002.
- Berry, A. J., J. Hermann, H. S. C. O'Neill, and G. J. Foran  
2005 Fingerprinting the Water Site in Mantle Olivine. *Geology* 33(11). WOS:000233059000008: 869–872.
- Berry, A. J., A. M. Walker, J. Hermann, et al.  
2007 Titanium Substitution Mechanisms in Forsterite. *Chemical Geology* 242(1–2). WOS:000248433400010: 176–186.
- Blanchard, Marc, Jannick Ingrin, Etienne Balan, István Kovács, and Anthony C. Withers  
2017 Effect of Iron and Trivalent Cations on OH Defects in Olivine. *American Mineralogist* 102(2): 302–311.
- Chen, Y., A. Provost, P. Schiano, and N. Cluzel  
2011 The Rate of Water Loss from Olivine-Hosted Melt Inclusions. *Contributions to Mineralogy and Petrology* 162(3). WOS:000294216500011: 625–636.
- Demouchy, S., and S. Mackwell  
2003 Water Diffusion in Synthetic Iron-Free Forsterite. *Physics and Chemistry of Minerals* 30(8). WOS:000185964900006: 486–494.
- 2006 Mechanisms of Hydrogen Incorporation and Diffusion in Iron-Bearing Olivine. *Physics and Chemistry of Minerals* 33(5). WOS:000240439000005: 347–355.
- Demouchy, Sylvie, and Nathalie Bolfan-Casanova  
2016 Distribution and Transport of Hydrogen in the Lithospheric Mantle: A Review. *Lithos* 240: 402–425.
- Demouchy, Sylvie, Catherine Thoraval, Nathalie Bolfan-Casanova, and Geeth Manthilake  
2016 Diffusivity of Hydrogen in Iron-Bearing Olivine at 3 GPa. *Physics of the Earth and Planetary Interiors* 260: 1–13.
- Faul, Ulrich H., Christopher J. Cline II, Emmanuel C. David, Andrew J. Berry, and Ian Jackson  
2016 Titanium-Hydroxyl Defect-Controlled Rheology of the Earth's Upper Mantle. *Earth and Planetary Science Letters* 452: 227–237.
- Ferguson, David J., Helge M. Gonnermann, Philipp Ruprecht, et al.

2016 Magma Decompression Rates during Explosive Eruptions of Kīlauea Volcano, Hawaii, Recorded by Melt Embayments. *Bulletin of Volcanology* 78(10): 71.

Ferriss, E.

2015 Pynams: A Python Package for Interpreting FTIR Spectra of Nominally Anhydrous Minerals (NAMs). New York. <https://github.com/EFerriss/pynams>.

Ferriss, E., T. Plank, D. Walker, and M. Nettles

2015 The Whole-Block Approach to Measuring Hydrogen Diffusivity in Nominally Anhydrous Minerals. *American Mineralogist* 100(4). WOS:000352175700017: 837–851.

Ferriss, Elizabeth, Terry Plank, and David Walker

2016 Site-Specific Hydrogen Diffusion Rates during Clinopyroxene Dehydration. *Contributions to Mineralogy and Petrology* 171(6): 1–24.

Gaetani, G. A., J. A. O’Leary, N. Shimizu, Claire E. Bucholz, and Matthew Newville

2012 Rapid Reequilibration of H<sub>2</sub>O and Oxygen Fugacity in Olivine-Hosted Melt Inclusions. *Geology* 40(10): 915–918.

Hauri, E.

2002 SIMS Analysis of Volatiles in Silicate Glasses, 2: Isotopes and Abundances in Hawaiian Melt Inclusions. *Chemical Geology* 183(1–4). WOS:000174332300008: 115–141.

Ingrin, J., J. Liu, C. Depecker, et al.

2013 Low-Temperature Evolution of OH Bands in Synthetic Forsterite, Implication for the Nature of H Defects at High Pressure. *Physics and Chemistry of Minerals* 40(6). WOS:000319771000005: 499–510.

Jollands, Michael C., José Alberto Padrón-Navarta, Jörg Hermann, and Hugh St.C. O’Neill

2016 Hydrogen Diffusion in Ti-Doped Forsterite and the Preservation of Metastable Point Defects. *American Mineralogist* 101(7): 1560–1570.

Keppler, Hans, and Joseph R. Smyth

2006 Water in Nominally Anhydrous Minerals, vol.62. *Reviews in Mineralogy and Geochemistry*. Mineralogical Society of America.

Kohlstedt, D. L., and S. J. Mackwell

1998 Diffusion of Hydrogen and Intrinsic Point Defects in Olivine. *Zeitschrift Fur Physikalische Chemie-International Journal of Research in Physical Chemistry & Chemical Physics* 207. WOS:000076569300010: 147–162.

Kurosawa, M., H. Yurimoto, and S. Sueno

1997 Patterns in the Hydrogen and Trace Element Compositions of Mantle Olivines. *Physics and Chemistry of Glasses* 24: 385–395.

Le Voyer, Marion, Paul D. Asimow, Jed L. Mosenfelder, et al.

2014 Zonation of H<sub>2</sub>O and F Concentrations around Melt Inclusions in Olivines. *Journal of Petrology* 55(4): 685–707.

Libowitzky, E., and G. R. Rossman  
1996 Principles of Quantitative Absorbance Measurements in Anisotropic Crystals. Physics and Chemistry of Minerals 23(6). WOS:A1996VD85000001: 319–327.

Lloyd, Alexander S., T. Plank, Philipp Ruprecht, E. H. Hauri, and William Rose  
2013 Volatile Loss from Melt Inclusions in Pyroclasts of Differing Sizes. Contributions to Mineralogy and Petrology 165: 129–153.

Mackwell, S. J., and D. L. Kohlstedt  
1990 Diffusion of Hydrogen in Olivine - Implications for Water in the Mantle. Journal of Geophysical Research-Solid Earth and Planets 95(B4). WOS:A1990CZ37500052: 5079–5088.

Mironov, Nikita, Maxim Portnyagin, Roman Botcharnikov, et al.  
2015 Quantification of the CO<sub>2</sub> Budget and H<sub>2</sub>O–CO<sub>2</sub> Systematics in Subduction-Zone Magmas through the Experimental Hydration of Melt Inclusions in Olivine at High H<sub>2</sub>O Pressure. Earth and Planetary Science Letters 425: 1–11.

Mosenfelder, J. L., N. I. Deligne, P. D. Asimow, and G. R. Rossman  
2006 Hydrogen Incorporation in Olivine from 2–12 GPa. American Mineralogist 91(2–3). WOS:000235472000007: 285–294.

Padrón-Navarta, Jose Alberto, Joerg Hermann, and Hugh St. C. O'Neill  
2014 Site-Specific Hydrogen Diffusion Rates in Forsterite. Earth and Planetary Science Letters 392: 100–112.

Peslier, A. H., and J. F. Luhr  
2006 Hydrogen Loss from Olivines in Mantle Xenoliths from Simcoe (USA) and Mexico: Mafic Alkalic Magma Ascent Rates and Water Budget of the Sub-Continental Lithosphere. Earth and Planetary Science Letters 242(3–4). WOS:000235855100006: 302–319.

Portnyagin, M., Renat Almeev, S. Matveev, and Francois Holtz  
2008 Experimental Evidence for Rapid Water Exchange between Melt Inclusions in Olivine and Host Magma. Earth and Planetary Science Letters 272: 541–552.

Rosen, Julia  
2016 Crystal Clocks. Science 354(6314): 822–825.

Ruprecht, Philipp, and Terry Plank  
2013 Feeding Andesitic Eruptions with a High-Speed Connection from the Mantle. Nature 500(7460): 68–72.

Shuai, Kang, and Xiaozhi Yang  
2017 Quantitative Analysis of H-Species in Anisotropic Minerals by Polarized Infrared Spectroscopy along Three Orthogonal Directions. Contributions to Mineralogy and Petrology 172(2–3): 14.

Thoraval, Catherine, and Sylvie Demouchy

2014 Numerical Models of Ionic Diffusion in One and Three Dimensions: Application to Dehydration of Mantle Olivine. *Physics and Chemistry of Minerals* 41(9). WOS:000341924800005: 709–723.

Tollan, P. M. E., H. St C. O'Neill, J. Hermann, A. Benedictus, and R. J. Arculus

2015 Frozen Melt-Rock Reaction in a Peridotite Xenolith from Sub-Arc Mantle Recorded by Diffusion of Trace Elements and Water in Olivine. *Earth and Planetary Science Letters* 422. WOS:000355350700018: 169–181.

Tollan, Peter M. E., Rachel Smith, Hugh St C. O'Neill, and Jörg Hermann

2017 The Responses of the Four Main Substitution Mechanisms of H in Olivine to H<sub>2</sub>O Activity at 1050 °C and 3 GPa. *Progress in Earth and Planetary Science* 4(1): 14.

Withers, A. C.

2013 The Pitzer and Stern Equation of State for Water.

<http://www.geo.umn.edu/people/researchers/withe012/fugacity.htm>, accessed August 6, 2013.

Withers, Anthony C, Hélène Bureau, Caroline Raepsaet, and Marc M Hirschmann

2012 Calibration of Infrared Spectroscopy by Elastic Recoil Detection Analysis of H in Synthetic Olivine. *Chemical Geology* 334: 92–98.

Zhao, Y. H., S. B. Ginsberg, and D. L. Kohstedt

2004 Solubility of Hydrogen in Olivine: Dependence on Temperature and Iron Content.

*Contributions to Mineralogy and Petrology* 147(2). WOS:000221169500003: 155–161.